8-2019

A Numerical Study of the Scaling and Control of Crossing Shock-Wave/Turbulent Boundary-Layer Interactions

Matthew Schwartz
University of Tennessee

Recommended Citation

Schwartz, Matthew, "A Numerical Study of the Scaling and Control of Crossing Shock-Wave/Turbulent Boundary-Layer Interactions. " Master's Thesis, University of Tennessee, 2019.
https://trace.tennessee.edu/utk_gradthes/5670

To the Graduate Council:

I am submitting herewith a thesis written by Matthew Schwartz entitled "A Numerical Study of the Scaling and Control of Crossing Shock-Wave/Turbulent Boundary-Layer Interactions." I have examined the final electronic copy of this thesis for form and content and recommend that it be accepted in partial fulfillment of the requirements for the degree of Master of Science, with a major in Aerospace Engineering.

John Schmisseur, Major Professor

We have read this thesis and recommend its acceptance:

Ryan Bond

Accepted for the Council:
Dixie L. Thompson

Vice Provost and Dean of the Graduate School

(Original signatures are on file with official student records.)

A Numerical Study of the Scaling and Control of Distortion Caused by Crossing Shock-Wave/Turbulent Boundary-Layer Interactions

A Thesis Presented for the
Master of Science
Degree
The University of Tennessee, Knoxville

Matthew Joseph Schwartz
August 2019

ACKNOWLEDGEMENTS

I would like to sincerely thank my advisor, Dr. John Schmisseur, for his guidance and mentorship. His advice, understanding, and kindness has made this entire process so much easier. I would also like to thank Dr. Ryan Bond and Dr. Ryan Glasby for all of their mentorship and patience when I came to them with questions, both academic and professional. A special thank you also goes to Stefen Lindörfer; he taught me the basics of graduate school survival as well as CFD. I truly do not think I would be a computationalist if it weren’t for him. I’d also like to thank Dr. James Coder and Dr. Trevor Moeller in addition to Dr. Schmisseur and Dr. Bond for serving on my committee. Dr. Phillip Kreth and Dr. Mark Gragston, whose enormous amount of both technical and emotional support, are dearly appreciated. I’d like to acknowledge Katherine Stamper for her willingness to perform the validation experiments. Finally, I’d like to thank the rest of the HORIZON research group for seeing me through to the end of this process.

ABSTRACT

To improve the design process of hypersonic vehicles, the performance of high-speed inlets must be evaluated through their entire flight domain. Hypersonic inlets are optimized for cruise conditions, but off-design operation introduces significant sources of uncertainty. Although many studies of high-speed inlets exist, much work is still needed in understanding the uncertainty associated with extrapolating ground test data to true flight conditions. Many ground facilities can match flight Mach numbers; however, many of these facilities are limited in Reynolds number ranges and matching true flight temperatures is difficult without vitiating the air.

To assist in understanding the uncertainty associated with these experimental complications, the present study conducted a numerical campaign observing the effects of scaling Reynolds number, stagnation temperature, and gas and wall thermal models on high-speed, crossing-shock-wave/boundary-layer interactions. The interaction was generated by two symmetric, sharp fins, and this geometry is intended to be representative of high-speed inlets. The primary flow feature observed was the distortion levels downstream of the interaction. Distortion is difficult to measure experimentally and is a commonly observed metric determining the performance of an inlet. It was found that distortion decreased with an increase in Reynolds number and compressible shape factor of the incoming flow.

The performance of vortex generators in passively controlling this interaction was also studied. These devices were shown to delay separation, however they also increased distortion levels at the outlet, and induced momentum losses compared to the baseline case without flow control.

TABLE OF CONTENTS

LIST OF FIGURES

CHAPTER ONE

INTRODUCTION AND MOTIVATION

A significant challenge in the development of high speed vehicles is the difficulty of establishing stable, air-breathing propulsion systems [1]. Ramjets and scramjets have been the subject of extensive research; however, massive flow separation caused by interactions between shock waves and boundary layers within the inlets of such systems leads to decreased performance and possible engine failure [2,3]. These shock-wave/boundary-layer interactions (SBLI) also contribute to increased total pressure losses and flow distortion [4]. This flow degradation can potentially unstart the inlet as seen with the X-51 flight tests [5], and the thermal and acoustic loads created by these interactions can be catastrophic to the vehicle's structural integrity [6,7]. To ensure vehicle reusability and minimize losses, a better understanding of SBLI and their role in unstart is required.

These interactions have been extensively studied over several decades, but few studies have focused on the influence of wall thermal conditions on turbulent SBLI [8,9]. These few existing studies have suggested that the influence of these thermal conditions may be significant, and wall cooling could potentially be used as a flow control method. These studies focused primarily on how the thermal wall boundaries affect the scale of the interaction. There is a gap in the literature on how thermal conditions and local Reynolds number affect total flow distortion, which has been studied as a characteristic of performance in high-speed inlets [10–13].

An objective of the present study is to determine how scaling thermal conditions and Reynolds number will impact the distortion of the bulk flowfield. The reason the scaling of these factors is of interest is because of how they relate ground tests to flight tests. Wind tunnel experiments are widely used to predict flight conditions. They are undoubtedly extremely beneficial, but they are not without their flaws. These ground facilities are often limited in the flow conditions they can create, which may introduce uncertainties when attempting to extrapolate wind tunnel results to flight conditions. One source of epistemic uncertainty encountered in extrapolating ground tests' results to flight is the difference in stagnation pressures and temperatures. It is standard practice for a wind tunnel facility to attempt to match flight Reynolds numbers (*Re*); however, this is often done by increasing the stagnation pressure (P_0) of the wind tunnel facility, thus causing a discrepancy between test and flight stagnation pressures. Since nozzles in ground testing facilities isentropically expand air to reach flight Mach numbers (M), static temperatures (T) in ground tests are much lower than flight conditions as a result; it is difficult for wind tunnel facilities to match flight stagnation (T_0) and static temperatures. Air is occasionally heated for ground tests, however this may change the properties of the air which may add an additional source of uncertainty.

These discrepancies result in a significant difference between flight and ground pressures and temperatures, even when Mach numbers and Reynolds numbers are matched. This inconsistency grows with increasing Mach numbers. In addition to flow temperature differences in many ground tests, wall temperatures may be colder than flight for short test times or hotter than flight for uncooled models in continuous tests. Different wall temperatures introduce additional uncertainty in extrapolating ground tests to flight conditions.

To better understand uncertainties as they relate to ground-to-flight extrapolation of hypersonic inlet studies, the current work will numerically study the influence of wall temperatures, free stream temperatures, and free stream Reynolds number on the bulk flow distortion of crossing shock-wave/turbulent boundary layer interactions (SWTBLI) generated by a double-fin. A double-fin geometry is used as a canonical, high-speed inlet-like configuration and has been recognized as a geometry to be studied for fundamental SBLI analysis [14]. As previous studies focused primarily on the size and scale of an oblique SBLI [8,9], this study will investigate how parametric scaling of these interactions may distort the flow field. Different gas models and thermal wall boundary conditions, such as general, adiabatic, and isothermal wall boundary conditions, are employed to help determine the uncertainty associated with common computational approximations. Many numerical studies use adiabatic walls and a perfect gas model when studying these types of flow fields. This study will explore the error introduced by these simplifications.

In addition to providing a better understanding of flow distortion, the current study also aims to identify strategies to reduce it. The distortion control effectiveness of passive flow control devices, specifically, micro vortex generators (VG) will be studied numerically.

CHAPTER TWO

LITERATURE REVIEW

As mentioned in the first chapter, the shock generator modeled in this study is a double-fin configuration. This geometry is representative of supersonic inlets, as it is a simplification of sidewall compression inlets, and it is a commonly studied canonical validation case for computational modeling of three-dimensional SBLI [15]. It is defined by a supersonic flow traveling towards an interior channel created by two (symmetric) semi-infinite fins. From the late 1980s into the early 2000s, a large amount of both experimental and computational work was invested to understand swept and crossing shock interactions, which have led to a significant number of reviews discussing the behavior and modeling of these flowfields [16–19]. Reynolds-averaged Navier-Stokes (RANS) simulations have been used to study this flow field and have been compared to experimental data [15]. RANS cannot predict the inherent unsteadiness of the interaction, but it has matched experimental surface flow visualizations and pressure measurements, suggesting that RANS is capable of modeling the mean flow with acceptable accuracy [15].

An extensive experimental study on the structure of this interaction was conducted by Settles and Garrison [20] and was included in an in depth review by Knight et al. [21]. Settles and Garrison visualized the complex shock structure through experimental planar laser scattering [20]. Knight et al. [21] organized many of these images to help visualize and explain the structure as can be seen in the three-dimensional perspective shown in Figure 2.1. Only half of the interaction is displayed as it is symmetric. The image shows flow at M_∞=4 over two symmetric fins with an angle of 15°. Three separate cross sections at various stream wise positions are also shown in the figure. The first cross section appears upstream of the collision between the two oblique shockwaves, thus it is equivalent to a single fin interaction. This structure is a traditional, turbulent SBLI, forming a “lambda” shock structure. There is the upstream separation shock, denoted by a

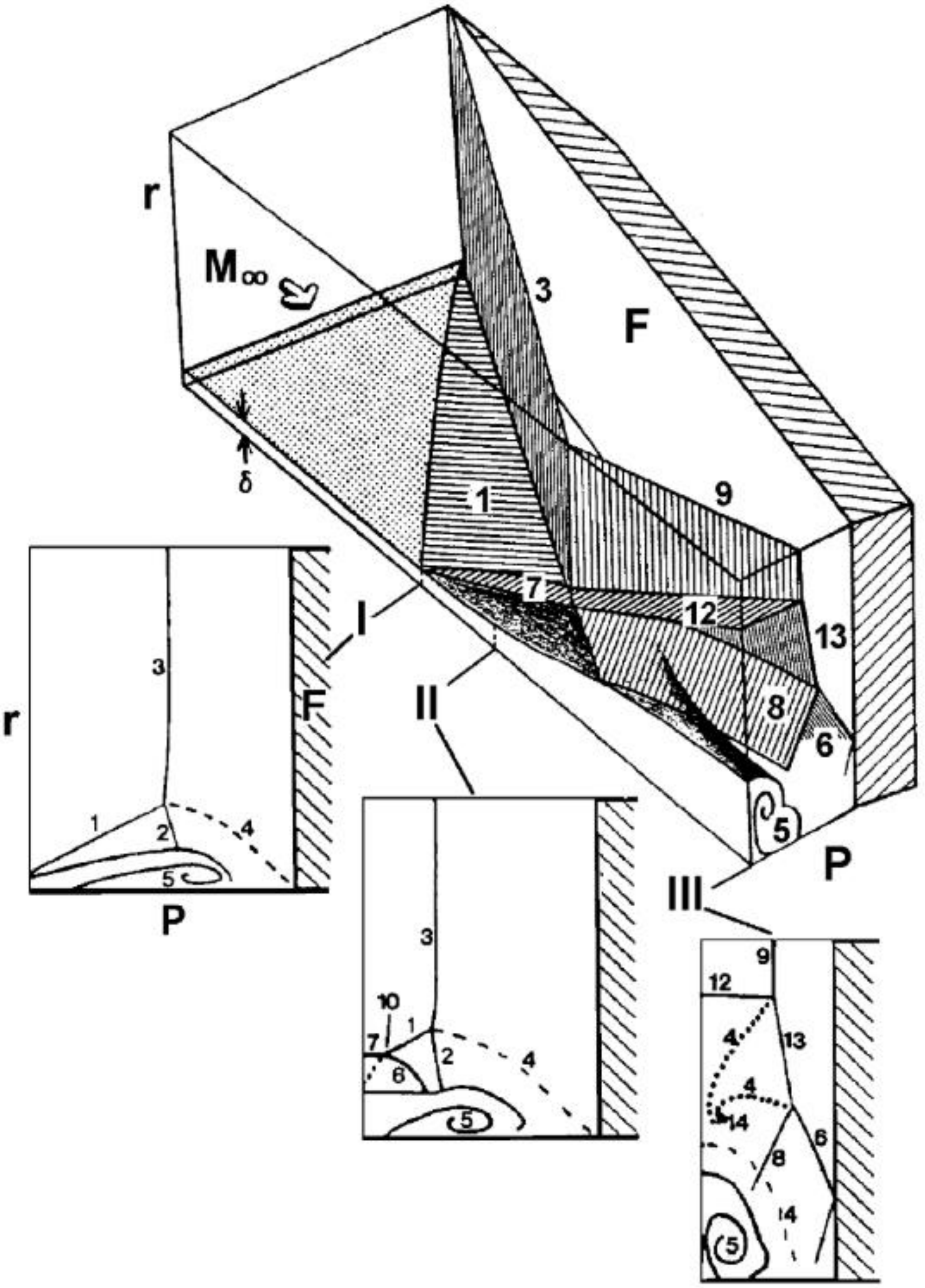

Figure 2.1 Double-fin flow structure at various streamwise locations [21].

“1”, as well as a rear shock wave, “2”. The shock wave labeled “3” is the inviscid shock that indicates the interaction. Downstream of the shockwaves is a slip line, “4”, emanating from the triple point. Label “5” is a separation vortex beneath the bifurcated shockwaves which form the lambda shock structure. The second cross-section corresponds to a location downstream of the collision. At this point the complexity of the interaction begins to show. Note that the vertical plane on the left side of this cross-section is the symmetry plane, which behaves as a perfect inviscid reflection plane. Structures 1-5, as described in the first shown cross-section, are the same. Additional downstream features at the second cross section include a reflected separation shock “6”, a straight shock resulting from the reflection “7”, which is also known as a Mach stem, and an additional triple point “10”. The third cross-section shows this lambda structure reflected non-uniformly from this symmetry plane. Additional slip lines have formed, consistently labeled “4”. A new shock, “12”, along the centerline appears bridged by the interaction with shock segment, “13”, connects the structure to a reflected inviscid shock wave, “9”. The reflected separation and rear shock waves, “6” and “8” respectively, are also connected by the bridge segment, “13”. The shock structure is complicated, and it may distort the flow field significantly. The interested reader may refer to the original papers, where more cross sections of the flow field can be seen [20,22,23].

Figure 2.2 are volume velocity stream ribbons and surface streamlines for the same interaction [24]. This figure displays the four coherent features of this flowfield. The first feature is that the boundary layer upstream fully separates from the surface labeled as “Separated Boundary layer” in the figure. The next feature is labeled the “Vortex interaction”. This vortex is located downstream of the fin leading edge, and it is seen to turn towards the centerline then separates from the separated boundary layer flow downstream. The third features is the “Centerline vortex”. This feature also originates near the leading edge of the fin, and also sweeps towards the centerline. The fourth feature is the “Entrainment flow”. This region behaves nearly inviscid, and it involves higher energy fluid attaching near

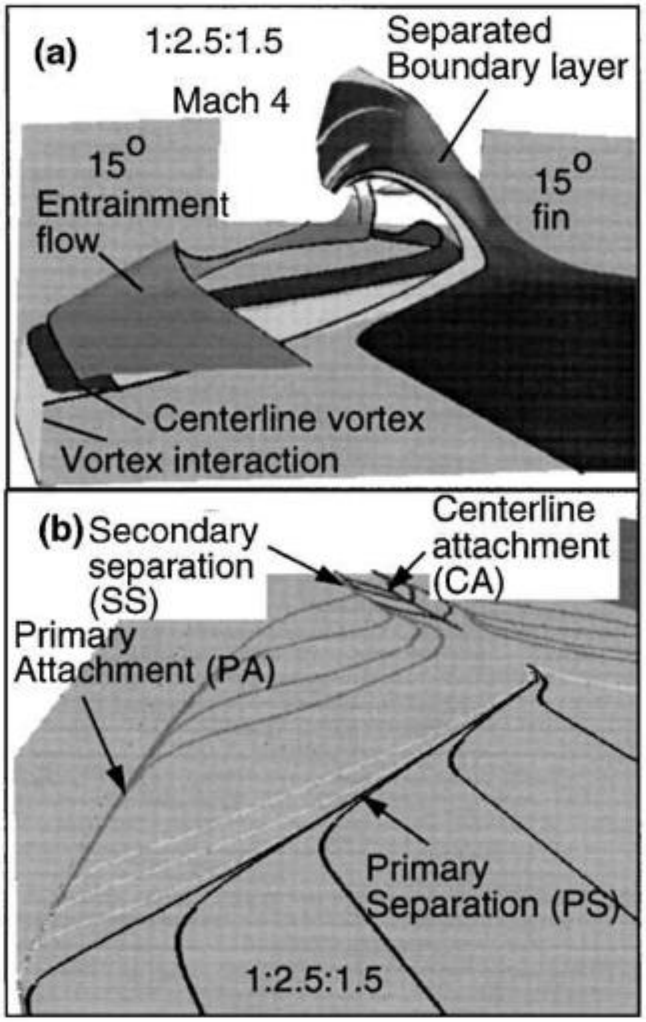

Figure 2.2 Coherent structures showing a) velocity streamribbons b) surface streamlines for a symmetric interaction [24].

the corner, but then separates before reaching the centerline. The result is a form of rotation countering that of the centerline vortex [24].

To better visualize how this interaction distorts the flow field, Figure 2.3 shows a half-symmetry plane of a double fin interaction. Numerical surface streamlines are plotted on the floor and cross-sections with stagnation pressure contour lines are places at various streamwise locations. These stagnation pressure contour lines illustrate qualitatively how the flow distorts. Each subsequent cross section in the stream wise direction is less uniform and exhibits increased losses in stagnation pressure. These stagnation pressure losses are greater at higher *Re* flows, and is discussed in later sections of the thesis.

There are two underlying factors that highlight the importance of understanding and characterizing this distortion. The first is to be able to understand the expected losses of the inlet. The second is many experimental and computational studies that look at isolators or combustors, which are located downstream of the inlet.

To model full field flow, the inflow to these conditions attempts to mimic the distorted flow that would be seen if there were an inlet upstream [11]. Many studies have been performed to attempt to generate flight like distortion conditions. Techniques to reproduce this distortion involve using different area blockages, air jets, screens, swept geometries, or a combination of these [25–27]. It is important, however, to understand the uncertainty associated with generating this distortion, as there may be blind or unquantified uncertainties associated with these flow fields [28]. Some of these uncertainties may stem from differences in ground and flight testing. One of the largest differences between ground facilities and flight conditions is temperatures. Static flow temperatures are significantly different between wind tunnels and flight conditions, and there are also differences in wall thermal conditions. Few experiments have looked at wall thermal conditions [29–31] and even fewer computational studies exist [8].

It was found that the effect of wall temperature can be more important than Reynolds number in the size of the interaction [8]. Granted this was for low

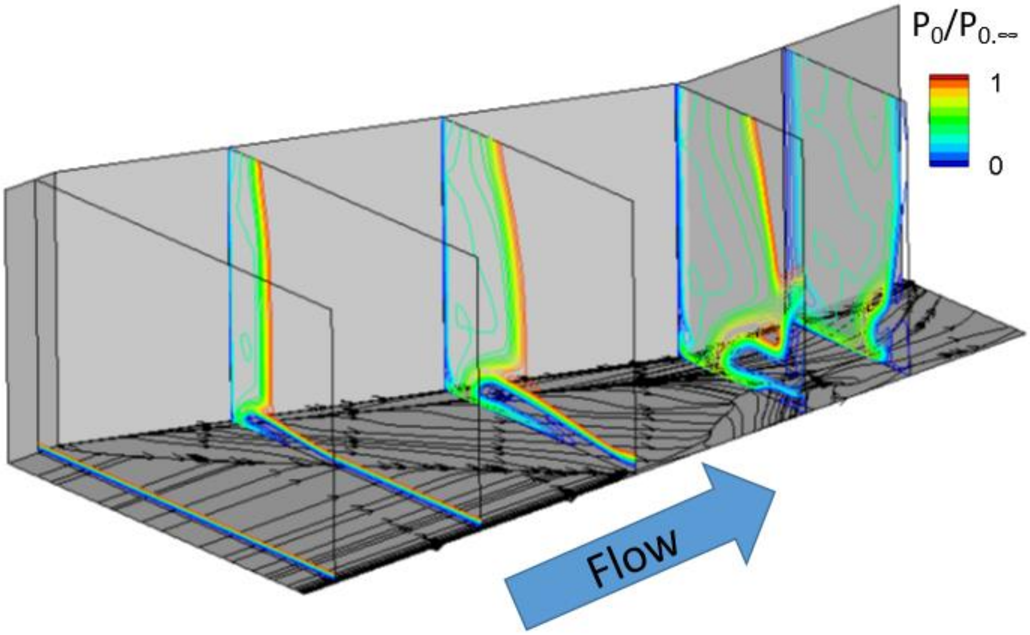

Figure 2.3 Surface streamlines and stagnation pressure contour lines.

Reynolds numbers, so this may not hold true at high Reynolds numbers, but it potentially is still significant. The focus of the mentioned studies was on oblique SBLI, and flow distortion was not the area of study. There appears to be a gap in the literature on how thermal conditions may affect crossing SBLI and bulk flow distortion. SBLI in inlets have detrimental effects beyond simply distorting the flow. Intense adverse pressure gradients on the surface are introduced by the shockwaves and result in significant boundary layer separation, which acts as area blockage to the flow field. This blockage is detrimental to performance, and in the worst case can even unstart the inlet [32–35].

Many flow control methods have been studied to reduce the scale of this separation. One of the more popular methods is boundary layer bleed. This method involves removing low momentum flow within the boundary layer near the wall; it has been shown to suppress separation, increase total pressure recovery, and reduce distortion [4,36,37]. Unfortunately, bleed systems are complex, add weight to a vehicle, and remove a considerable amount of mass flow from the inlet. Due to these detrimental effects, alternative flow control methods are desirable. The use of vortex generators (VGs) have been considered, as they may increase the momentum of flow near walls by introducing strong streamwise vortices. In many flow applications, VGs have been effective in controlling flow separation; however, they introduce additional parasitic drag and shockwaves in supersonic flows. To minimize this negative effect, vortex generators on the scale of the boundary layer thickness (δ) or smaller have been used [38–43]. These devices are referred to as micro vortex generators (MVGs, sometimes referred to as µVGs). Many numerical and experimental studies have shown the effectiveness of MVGs in reducing separation in SBLI [38–43], and have even specifically been looked at for the use in supersonic inlets [41,44,45]. In some cases, these MVGs may reduce the separation length by nearly 20% [46] and can reduce the maximum pressure within the separation zone by as much as 50% compared to the uncontrolled case [47]. Numerous different MVG geometries have been studied. The most common geometries are triangular ramps, vanes, and ramped-vanes

[48,49]. While they introduce slightly more parasitic drag than the other geometries, triangular ramps are more mechanically robust, allowing them to better withstand temperatures and pressures of supersonic flow conditions [46].

The work on the effect of vortex generators on SBLI separation is vast and growing; however, an understanding of their effects on influencing bulk flow distortion is lacking. When determining the height of VGs, the main trade off previous authors considered is the relationship between VG height, separation length, and drag introduction. It may be worth considering also how the use of MVGs effects outlet distortion, and that’s what this study attempts to do.

CHAPTER THREE

METHODOLOGY AND VALIDATION

All simulations were performed on high-performance workstations running the 64-bit versions of either Ubuntu 18.014.1 or 16.04.1. The machines had 256 GB RAM and 64 AMD Opteron™ Processors 6376 at 2300 MHz each. Pointwise V18.1R1 was used as a mesh generation tool and Tecplot 360 EX 2017 R2 was used for visualization and post-processing.

3.1 Numerical Setup and Flow Assumptions

3.1.1 Flow Field Assumptions

The fluid used for this study was standard atmosphere air. Air was treated to be a compressible, viscous, Newtonian fluid and either assumed to behave as a perfect gas or a calorically imperfect gas for specific cases. Sutherland's law [50] was used to calculate the dynamic viscosity (μ) of the air. Inflow conditions were assumed to be constant, and the flow path was determined to be at steady-state. Fluid flow for this study was presumed to be a continuum. All solid boundaries in these cases were modeled as being perfectly smooth, and corners and edges were modeled as being infinitely sharp.

3.1.2 Flow Solver Details

The HPCMP CREATE$^{\text{TM}}$-AV Kestrel flow solver component Kestrel CFD solver (KCFD) is used for the simulations of this work. KCFD is an unstructured, cell-centered, finite-volume code. KCFD permits parallel processing and allows different cell types within the same mesh. Second order spatial accuracy is achieved by calculating the spatial residual via a Godunov Scheme [51] with the usage of linear gradients in each cell. The HLLE++ scheme is used to solve the inviscid fluxes at each element face. Using a sub-iterative point-implicit scheme [52], second order temporal accuracy is available in the solver. The turbulence models used for this study are the one-equation Spalart-Allmaras turbulence model [53] with quadratic constitutive relations (QCR) [54] and the two-equation

Menter turbulence model [55], both a modified Menter baseline version and the shear-stress transport (SST) correction. All solutions are spatially second-order accurate and used 3 subiterations.

3.2 Capability Assessment

3.2.1 Profile Boundary Condition Assessment

The accuracy of KCFD's implementation of QCR and its profile boundary condition was examined before utilizing it for the goals of the present study. The profile boundary condition of KCFD allows a user to define a one-dimensional profile as an inflow condition. The user specifies a direction, time, spatial location, pressure, temperature, eddy viscosity ratio, turbulence intensity, Mach number, angle of attack, and sideslip values to the profile. This then sets the conditions for an inflow. This boundary condition can be utilized to minimize the size of a computational domain, as boundary layer profiles can be imposed instead of calculated. This allows for a smaller upstream domain.

As the present study aimed to match experimental wind tunnel data, an incoming boundary layer profile on the floor of the simulations must match the experimental boundary layer profile. This criterion could be met by simulating the entirety of the wind tunnel floor for each case; however, this is undesirable as it adds unnecessary computational expense. With the use of KCFD's profile boundary condition, a two-dimensional flat plate case was all that was needed to be simulated. This flat plate case was run until the desired boundary layer profile was generated. The flow variables were then extracted in the wall normal direction at the stream wise distance where the desired profile was met. To validate that this profile would continue to develop naturally when used as an inflow in a separate simulation, the extracted profile was then used as the input into the second simulation utilizing the profile boundary condition. The primary turbulent variables between the two simulations were compared at three locations as illustrated in Figure 3.1. The location where the variables were extracted in the source case is denoted as “0 cm”.

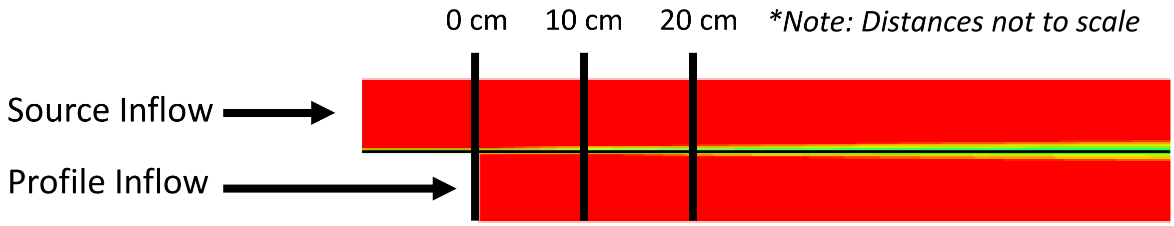

Figure 3.1 Extraction locations for source and profile inflow of the flat plate cases.

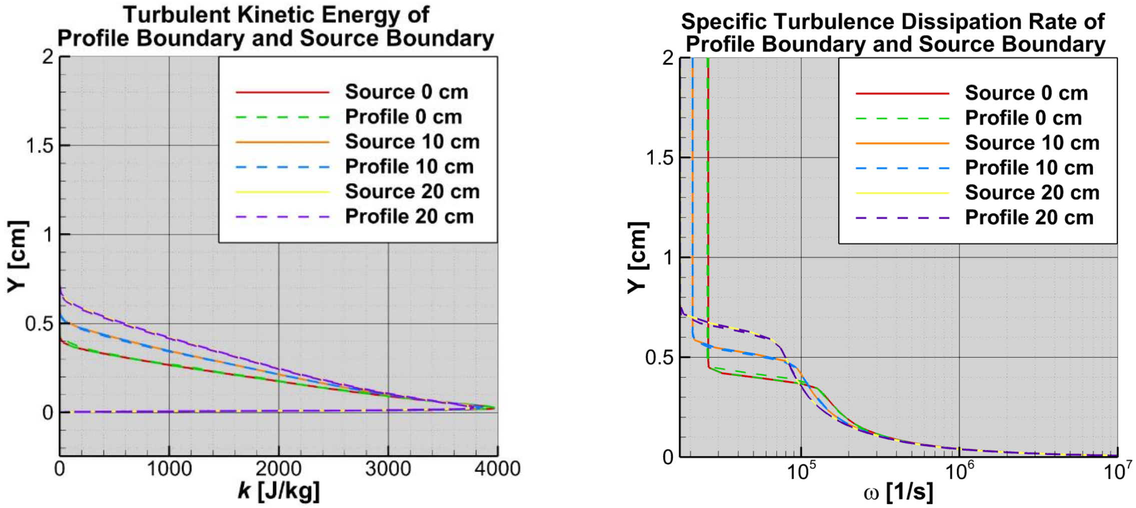

Figure 3.2 Comparison of k and ω between source and profile inflow boundary conditions.

For comparison, the domain of the profile boundary condition case has been shifted such that the inflow is at this same location. To ensure this boundary condition did not affect boundary layer development, flow variables were also extracted 10 cm and 20 cm downstream of this point in both cases for comparison. The turbulent kinetic energy (*k*) and the specific turbulence dissipation rate (ω) of each extraction against wall normal distance (*Y*) are compared in Figure 3.2. At each of the three locations, both *k* and ω between the two cases were identical within machine error. This instilled confidence that the profile boundary condition is behaving as expected.

3.2.2 QCR Validation

It has been shown that eddy viscosity turbulence models do not properly model secondary vortical flows near wall junctions or corners for internal flows [54]. As the current study will be looking at internal flow, corner flow is present and must be properly predicted. To address this issue, the quadratic constitutive relation (QCR) has been added to several turbulence models [54]. Kestrel has this QCR model in its Menter turbulence model implementation.

To determine the ability of Kestrel to properly model corner regions, a duct case was simulated to match existing experimental data. This case is listed on NASA's turbulence modeling resource page as a supersonic square duct validation case [56]. The domain of this study involved a square duct with a height and width D = 25.4 mm. The length (x) of the duct is x/D = 50 [57]. The grid for the numerical domain was a quarter-symmetry involving 481 cells equally spaced in the streamwise direction and 81 cells in both wall normal directions. All walls had a set wall distance so *a priori* estimates predicted $y^+ < 1$.

The baseline Menter turbulence model with and without the addition of QCR was used. The results of the experimental data are plotted in Figure 3.3 [57] against the computational results. The plot shows velocity versus wall normal distance in the *z* direction where the local velocity (*U*) is normalized by the

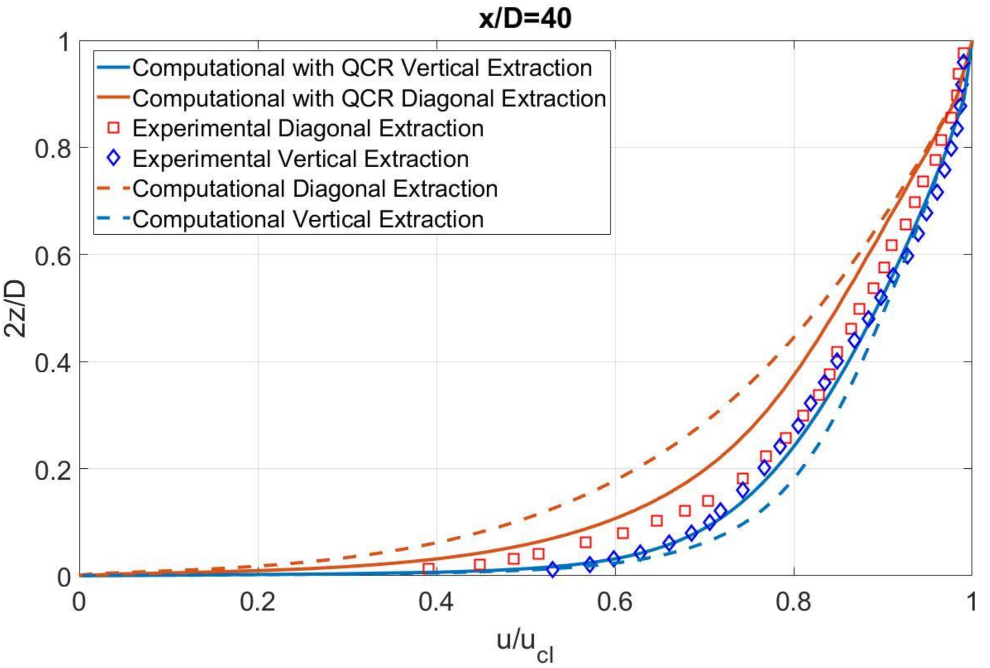

Figure 3.3 Experimental and computational velocity comparison in a supersonic square duct at x/D=40.

centerline velocity (U_{cl}) and twice the wall normal distance in the z direction is normalized by the duct width (D). Velocity data are plotted for two separate extractions. The "vertical" extraction was taken across the symmetry plane in the z-wall normal direction. The "diagonal" extraction was taken from the corner where the two walls meet to the centerline of the tunnel, which is where the two symmetry planes meet.

The computational results agree with the experimental results to an acceptable degree, with the implementation of QCR outperforming the baseline model. The mean absolute percentage difference between the experiments and computational results is 1.62% and 34.6% for the vertical and diagonal extractions respectively. Although the diagonal extraction does have a higher difference, the trend still is very similar, and it performs better than the model without QCR. The Menter baseline turbulence model with QCR was used for the remainder of the present study due to its superior performance.

3.3 Computational Domains and Validation

3.3.1 Flat Plate

To ensure a consistent incoming boundary layer thickness with continuous thermal and velocity profiles for each case, a simple, two-dimensional flat plate case was simulated for each condition in the test matrix. At each point in the test matrix, a separate flat plate simulation was run until the desired boundary layer thickness was reached. At this point, a profile was extracted in the wall normal direction to be used as an inflow to other cases using the profile boundary condition described in the previous section. The flat plate was a two-dimensional, fully hexahedral mesh with an *a priori* estimated non-dimensional wall distance $y^+ < 1$, and a specified growth rate of 1.2. This y^+ value was selected as it is a commonly used spacing for these types of flows [58,59]. The domain was 10m long and 0.125m tall. This length was enough to generate the desired boundary layer thickness of only 0.038m. The grid was over resolved and longer than necessary, but the total grid only had ≈350,000 cells so it was still inexpensive to run.

A no-slip, adiabatic wall boundary condition (BC) was enforced on the floor, a farfield BC was enforced on the upper surface, and a sink BC was used at the outflow. The static pressure for the sink BC was 80% of the inflow pressure to ensure that the outflow pressure was lower than the pressure within the domain.

3.3.2 Mach 4.961 Double Fin

The double fin configuration consisted of two symmetric fins with a 23° angle. The geometry was based on available experimental and computational cases [15,60] for validation purposes. The geometry and mesh resolution study outlined by Schmisseur and Gaitonde was used for the mesh of the current study [15]. The geometry extends 282mm in the streamwise direction, 102mm in the wall normal direction, and 154mm in the spanwise direction. The incoming boundary layer thickness (δ) is the incoming boundary layer thickness which in this case is 3.8 mm. The generated domain was a fully hexahedral mesh with a *posteriori* non-dimensional wall distance y^+<1. This tight spacing was used as different thermal wall boundaries were studied, so thermal boundary layers needed to be resolved. Spacing identical to the wall spacing was also defined at geometry changes, specifically at the leading and trailing edges of the fins. A growth rate of 1.2 was specified for each of these boundaries.

The cell with maximum equiangle skewness of the mesh was only 0.26, with an average equiangle skewness of the mesh being less than 0.13, where a skewness <0.5 is ideal. The maximum and average included angle for all cells of this grid were 113.4° and 101.7° respectively. A symmetry plane was used to reduce computational time. The computational domain is shown in Figure 3.4, and the surface mesh is displayed in Figure 3.5. Solid walls are shaded in the figure and were modeled as no-slip walls with either an adiabatic or an isothermal condition, which is discussed in a later section. The inflow plane is located 6 boundary layer thicknesses upstream of the leading edge of the fin. The previously described profile BC was used at the inflow. The outflow BC was a static pressure sink. To ensure the outflow condition did not influence the area of interest, the

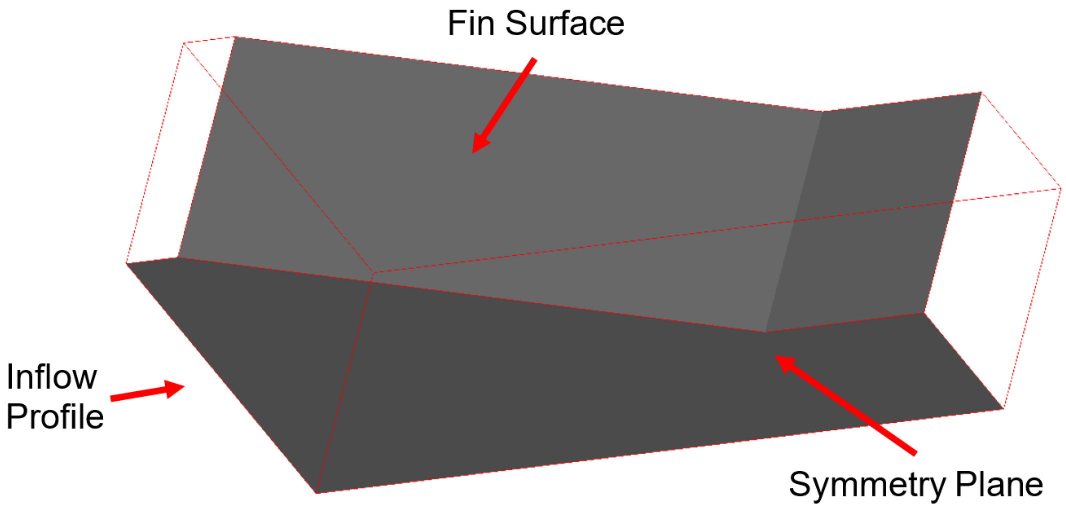

Figure 3.4 Computational domain of 23° degree double-fin.

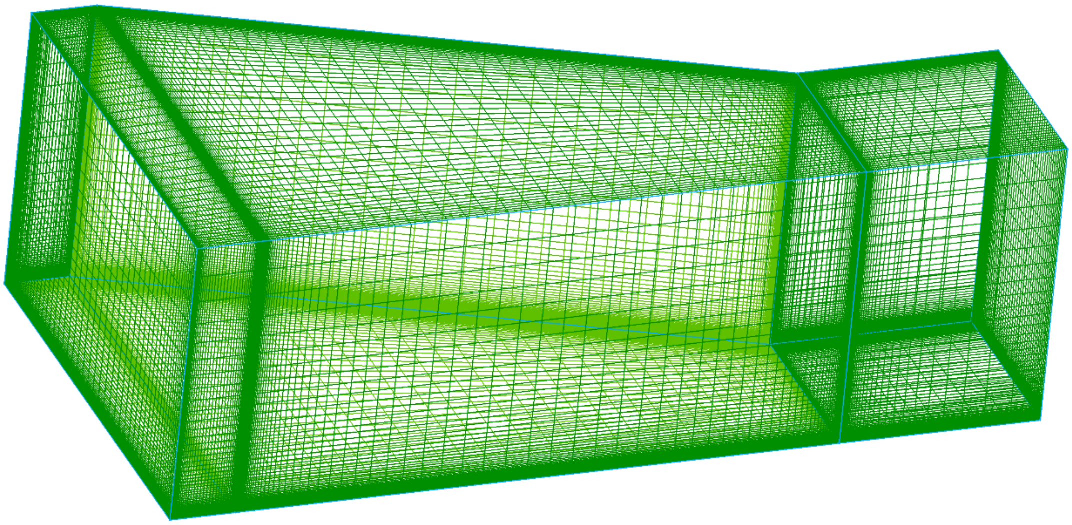

Figure 3.5 Surface mesh of the double-fin geometry.

static pressure was set to be 80% of the freestream pressure to prevent adverse pressure gradients near the outflow. Also, the outflow is located 25 boundary layer thicknesses downstream of the trailing edge of the fin to prevent the outflow pressure from affecting the areas of interest.

To validate the mesh and the ability of Kestrel to model this internal flow problem, a case identical to existing experimental data was simulated [60]. This involved a freestream Mach number and stagnation conditions of M=4.961, T_0=427 K, and P_0=2.2 MPa respectively. At these conditions, the freestream unit Reynolds number was 36.5×10^6 per meter or 138×10^3 based on δ. The aspect ratio of this study was 81, where the aspect ratio is defined as the distance between the leading edges of the fins divided by the incoming boundary layer thickness. A comparison between experimental and computational surface pressures are shown in Figure 3.6, where X denotes distance downstream of the fin leading edge and Z is the distance normal to the symmetrical centerline of the interaction nondimensionalized by δ. Pressure was nondimensionalized by the freestream pressure.

The first two plots, at $x=22.1\delta$ and $x=24.7\delta$, are upstream of the shock intersection. It is thus the simple, single-fin SBLI. The latter two plots, at $x=40.5\delta$ and $x=48.4\delta$, are downstream of the collision, and have slight discrepancies, particularly in the x=48.4δ comparison. Despite the minor disagreement near the shock collision, the plots support the claim that the current simulations accurately model the mean flowfield. Of all the plots, the x=40.5δ figure has the most discrepancy between experimental and computational results with a mean absolute percentage difference of 9.7%. At x=48.4δ mean absolute percentage difference was 6.6%. The remaining comparisons had a mean absolute percentage difference of less than 5%. The experimental data had a measurement uncertainty of ±5%.

To support this claim further, Figure 3.7 displays experimental surface streamlines [60] against numerical surface streamlines of the present study. In the images, lines of coalescence represent separation and are denoted with a script

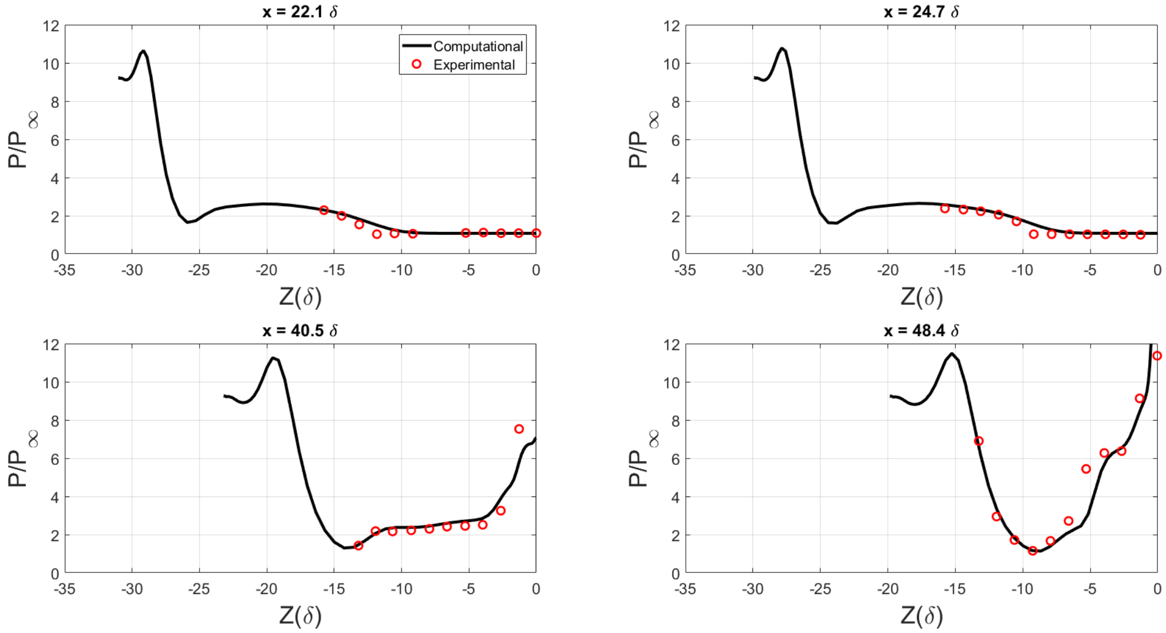

Figure 3.6 Surface pressure comparison between computations and experiments [60].

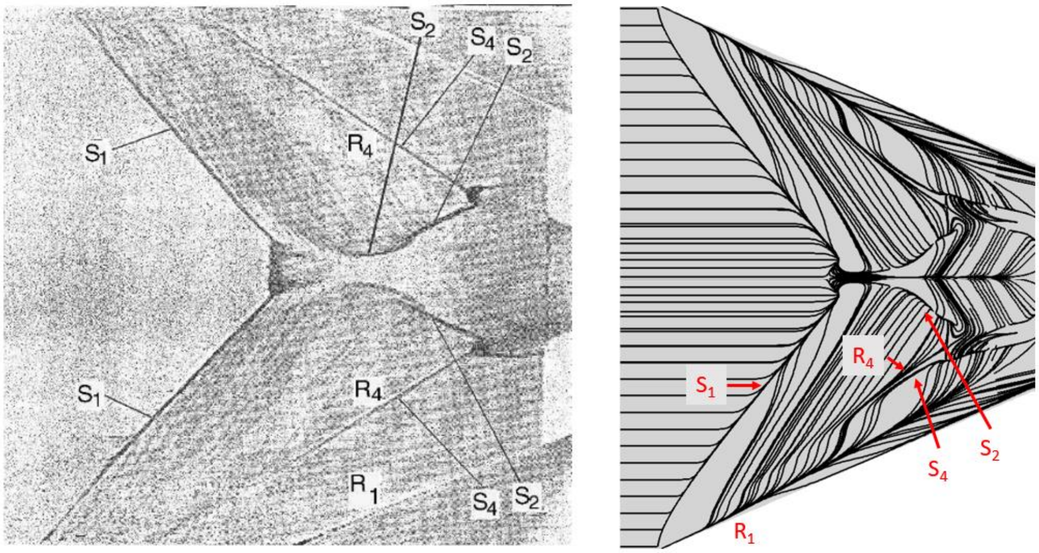

Figure 3.7 Experimental [60] and computational surface streamline comparison.

S. Lines of divergence represent attachment and are denoted with a label R. Numerical subscripts are used to distinguish separate features. Note that some numbers are skipped, specifically S_3, R_2, and R_3. In the experimental work, these features were present in previous figures for a separate interaction not reproduced in the present study; these features were not observed in the current interaction. To stay consistent with the comparing experimental nomenclature, the current work will skip these numbers as well. The flow features observed experimentally are accurately produced computationally.

The primary lines of separation and attachment, S_1 and R_1 respectively, are observed in similar locations in each case. Downstream of these structures, two mirroring lines of separation, S_2, are also consistent. Accompanying the primary attachment in each case is a secondary pair of separation and attachment, specifically S_4 and R_4. The numerical results agree with the experimental streamlines, thus implying that the simulations are capable of properly modeling this interaction.

3.3.3 Mach 2 Wind Tunnel

Additional simulations were performed to match complementary experiments performed in the Mach 2 blowdown wind tunnel at the University of Tennessee Space Institute (UTSI). This facility is a low-enthalpy facility with a 203 mm × 203 mm (8” × 8”) cross section. Standard air is the test gas supplied by a 23.6 m^3 bottle farm compressed to a maximum pressure of 20 MPa using a control valve to maintain a plenum pressure at approximately 240 kPa. The flow is unheated air, resulting in a stagnation temperature of 287 K. The freestream velocity and Mach number average 507 m/s and 2.01 respectively with a reported freestream unit Reynolds number of approximately 32×10^6 m^{-1} [62]. A turbulent boundary layer naturally develops on the floor of the wind tunnel with a thickness, δ, of approximately 11 mm in the area of interest [61]. A schematic of this facility is shown in Figure 3.8 [62].

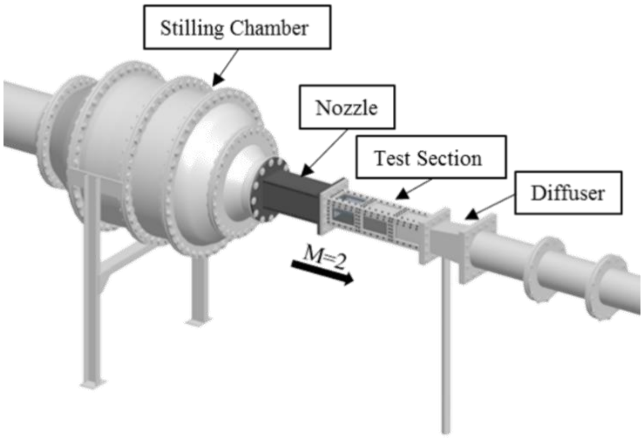

Figure 3.8 Schematic of UTSI Mach 2 facility [62].

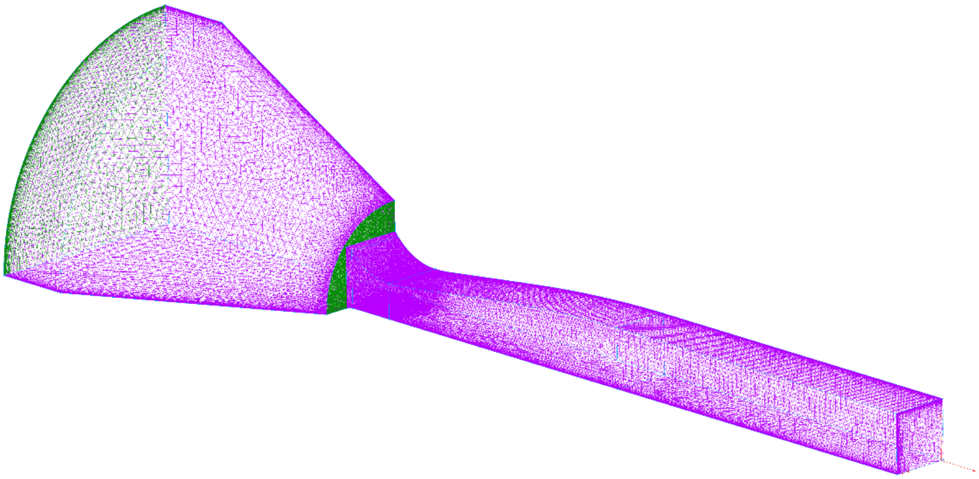

Figure 3.9 Quarter-symmetry mesh of the UTSI Mach 2 wind tunnel

To avoid simulating the entirety of the wind tunnel for each case, the facility was simulated once to generate a profile for the profile boundary condition described in Section 3.2.1. Only a quarter symmetry of the tunnel was simulated. Figure 3.9 is a surface mesh of the domain, including the stagnation chamber, nozzle, and test section. The mesh for the wind tunnel shown was an unstructured, tetrahedral mesh with quarter-symmetry. Adiabatic, no-slip walls were used on all the solid surfaces with an *a posteriori* y^+ value less than 1 on the nozzle and test section walls and a growth rate of 1.2. The inflow conditions were set to match the stagnation chamber conditions reported experimentally; with inflow total pressure (P_0) and total temperature (T_0) set to 240 kPa and 285 K respectively [63]. The outflow condition was a static pressure sink set to 80% of the freestream pressure. As with previously described simulations, this was to ensure adverse pressure gradients did not affect the area of interest.

For this simulation, the area of interest was the plane at the exit of the nozzle. To utilize the profile boundary condition previously alluded to, the primary flow variables were extracted at this location to be used as an inflow conditions for smaller domains in later cases.

A computational velocity profile is compared to an experimentally gathered velocity profile in the same facility. The experimental work used particle image velocimetry (PIV) to collect this data [62]. This comparison was performed to ensure that the facility was simulated properly. This comparison can be seen in Figure 3.10. Staying consistent with the nomenclature of the reference, the displayed variables are the velocity (U) normalized by the incoming freestream velocity (U_0) and the wall normal distance (Y) normalized by the boundary layer thickness (δ). The reported uncertainty of these measurements was 6.8% [59]. The PIV data lags slightly behind the computational data. A contributor to this discrepancy may be because PIV data is taken by tracking particles in the flow. These particles can lag slightly behind the fluid flow, causing measurements to be slightly lower than the true value. Additionally, comparing the shape factors between the two profiles showed that the computational profile is slightly more

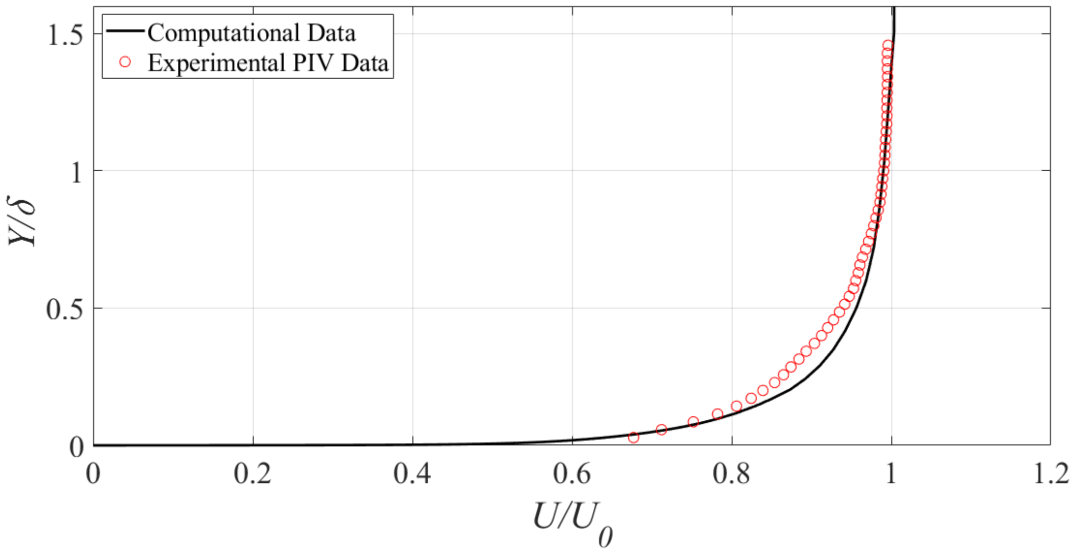

Figure 3.10 Computational and experimental velocity profile comparison.

developed with a shape factor of 1.20 and 1.21 for the computational and experimental profiles respectively. Note that since the experimental data did not report densities, these shape factors were calculated as if they were incompressible, which adds error to these calculations. There was only a 2.1% mean absolute percentage difference between the two plots, allowing the primary flow variables of the simulation to confidently be extracted and used for the other simulations that will be described later in the thesis.

3.3.4 Mach 2 Tunnel Fins

A double-fin configuration was also simulated at Mach 2. There were no existing experimental studies used for computational validation, so complimentary experiments were conducted for the present study. As such, the geometry of the Mach 2 interaction was constrained to what was allowable in the facility. The ideal geometry would not unstart the tunnel and would allow a regular shock reflection. The first design choice made was the angle of the fins. As a regular reflection was desired, a pressure deflection diagram was constructed using only the weak shock solutions. The chosen fin angle was 10° as this allows for a regular reflection as can be seen by the pressure deflection diagram shown in Figure 3.11, where Θ is the deflection angle and P is static pressure. Since a deflection at 10° results in a Mach number that is capable of turning the flow back to 0°, the plot suggests that a deflection at 10° will allow for a regular reflection with a factor of safety.

The height of the fins was set to 10δ to ensure the fins met the semi-infinite criteria [64].The length of the fins was determined geometrically by ensuring that the reflected shocks would not interact with the fin surface. This resulted in the half-symmetry geometry shown in Figure 3.12, where the orange surface is one of the two fins and the solid surfaces are the side walls and floor. The fin dimensions were 13.9δ in the streamwise direction, 2.3δ in the spanwise direction, and 10.4δ in the direction normal to the floor. The length of the fins was determined geometrically by ensuring that the reflected shocks would not interact with the fin surface. This resulted in the half-symmetry geometry shown in Figure 3.12.

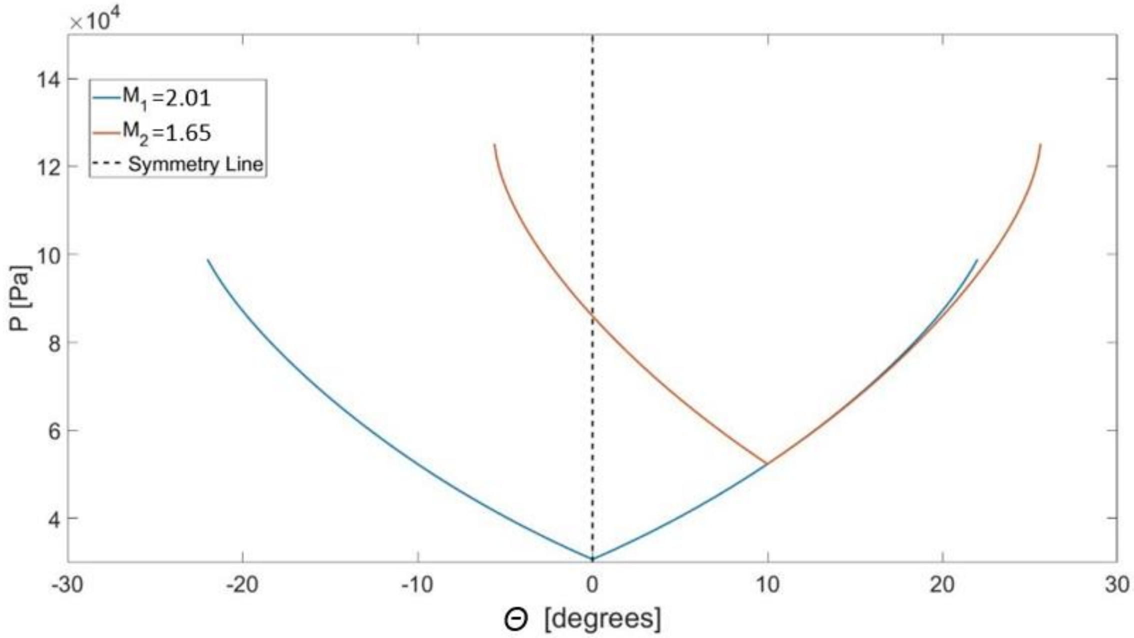

Figure 3.11 Pressure deflection diagram at $M_1=2$ with a deflection at $\Theta=10°$.

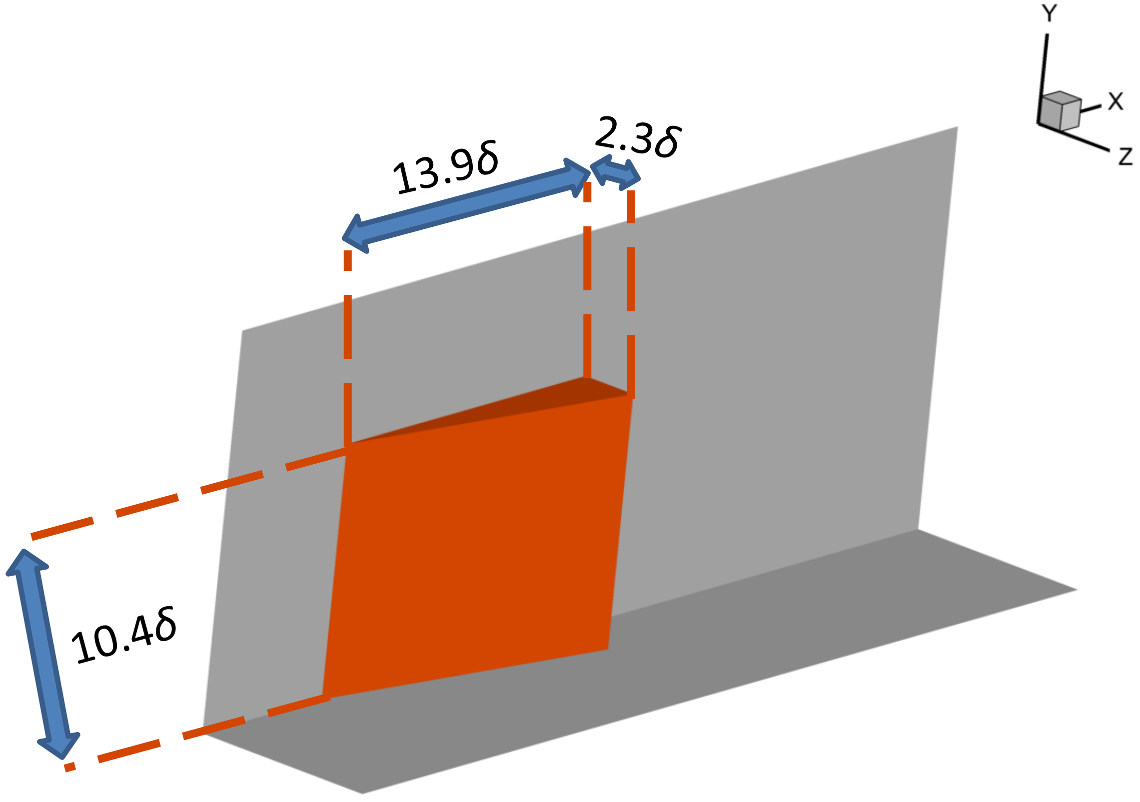

Figure 3.12 Schematic of half-symmetry of Mach 2 double fin configuration.

This fin geometry was used in the Mach 2 tunnel. To ensure that the tunnel would start and provide the desired flowfield, this domain was simulated using the inflow profile generated from the Mach 2 tunnel described in the previous section. Figure 3.13 displays the surface mesh of this domain, where the fin is colored orange. The mesh spacing was similar to that of the Mach 4.961 fins. Since this is a lower speed interaction, this mesh spacing should resolve this flowfield as well. The boundaries for this domain were slightly different than the Mach 4.961 domain as the flowfield of the top surface of the fin and the tunnel ceiling needed to be resolved.

This domain was half of the symmetric test section of the Mach 2 tunnel at UTSI with the fin geometry included. All other surfaces were adiabatic, no-slip walls. Like previous meshes in the study, a *posteriori* $y^+<1$ was observed for all solid boundaries and geometric changes with a growth rate of 1.2. This mesh is a hybrid grid with both structured and unstructured domains.

Due to the sharp nature of the fin, it was difficult to fit non-degenerate, structured cells within the 10° angle of the fin. As such, the surface domain was an unstructured mesh, using Pointwise's "T-rex" feature to resolve the edge. A closer look at the mesh of this surface is shown in Figure 3.14. This domain was extruded in the wall normal direction to create prism cells up to the top wall of the wind tunnel.

The inflow profile was set to be 6δ upstream to match existing computational work on similar geometries [15]. Like other simulations described previously, the outflow was set as a static pressure sink with a static pressure that was 80% of the freestream located 20δ downstream of the fin trailing edge.

The resulting computation showed that the model would not unstart the facility and that the shock structure reflects as expected. Figure 3.15 shows the domain in a similar style to Figure 3.12 with the addition of a pressure contour slice. Observing the contours, the tunnel is started, the shock structure contains a regular reflection, and the reflected shock does not interact with the body of the fin. Since this flowfield matched the design criteria, this fin geometry was made

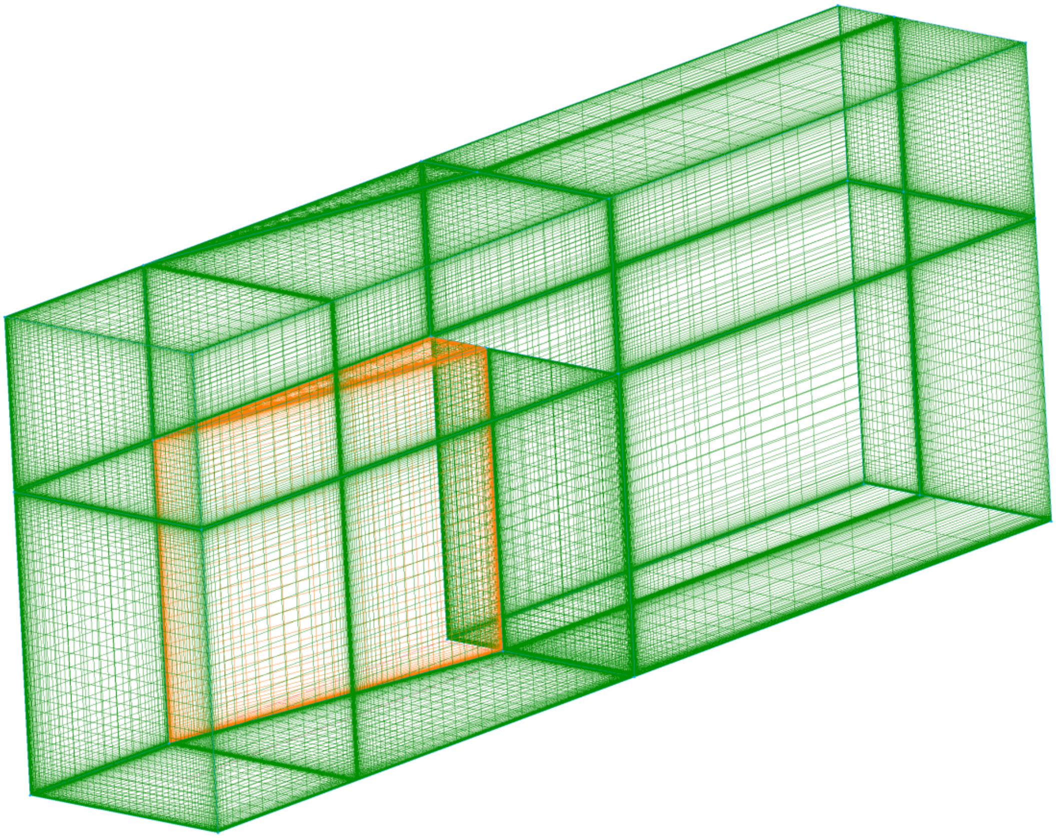

Figure 3.13 Surface mesh of Mach 2 tunnel Fin

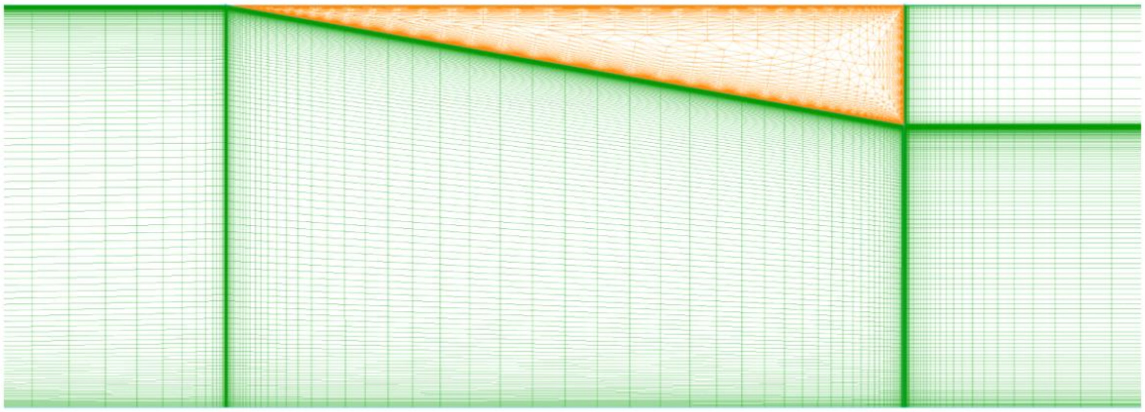

Figure 3.14 Top surface of a fin.

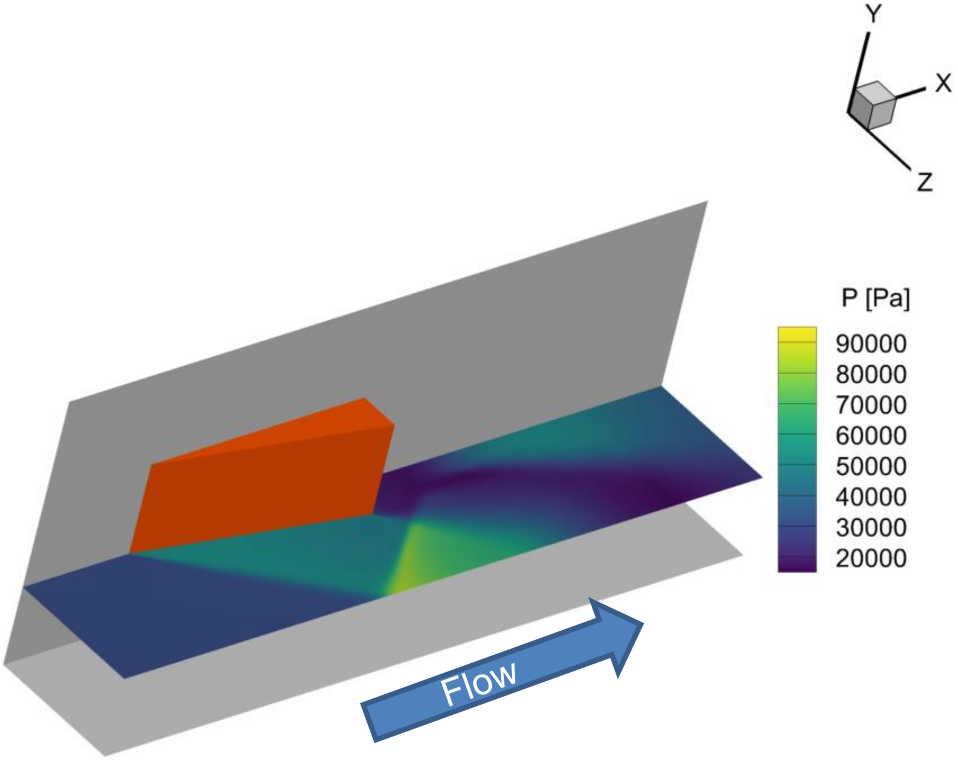

Figure 3.15 Pressure slice of Mach 2 double fin interaction.

into a physical model to be used for experiments in the wind tunnel. As no experiments of this geometry existed at the time of simulation, there was no available experimental validation. Experimental comparisons to similar simulations will be made later in the paper.

3.3.5 Vortex Generators

Vortex generators (VGs) were used to attempt to control distortion and separation in the Mach 2.01 interaction. There are several different VG geometries listed in the literature, but the ramped vane was selected due to its performance as well as its structural robustness [42,48]. The dimensions were selected based on the study of Lee et al [42], which define all the VG dimensions based on the VG height (*h*). There have been several studies discussing an ideal height for VGs [3,43,65], but all studies determined that increasing height will increase the effectiveness of the VGs in controlling flow separation; however, increased height will induce more drag and thus incur greater losses. It is thus suggested that for supersonic applications, the VG height should be smaller than the boundary layer thickness. For this reason, the present study selects an *h* that was 40% of the boundary layer thickness, which was approximately 4.4 mm; the VG length was 6.57*h* with a width of 5.48*h* based on the report of Lee et al. [42].

An experimental campaign was run prior to the computational work. Symmetric, aluminum wedges identical to the geometry described in the previous section were fabricated and attached to the side walls of the Mach 2 blowdown facility described in Section 3.3.3. The VGs were 3D printed out of acrylonitrile butadiene styrene (ABS) plastic which were adhered to the tunnel floor. Acetone was used to attempt to smooth the surfaces of the VGs as much as possible, but they were not perfectly smooth. The exact roughness measurement was not quantified. Surface oil flow visualization was used to capture the mean flow features, specifically separation topology. The aim of the experimental study was to determine an ideal location for the VGs regarding delaying separation.

The computational domain was based on the results of the experimental study and involved three vortex generators total. Figure 3.16 and Figure 3.17 display the surface mesh of the entire domain and a zoomed in view of the VG respectively. The surface of the VGs are colored orange to make them more apparent. For an inflow, this simulation used the profile generated in Section 3.3.3. The outflow used a static pressure sink set to 80% of the freestream pressure. To reduce computational expense, the top of the domain was truncated once the semi-infinite condition for this geometry was met. Since at this point, an increase in fin height would not alter the interaction, modeling the top surface of the fin and the rest of the tunnel was avoided. A farfield boundary condition was employed for this top domain. Walls were modeled as no slip, adiabatic walls.

Due to the difficult geometry, this mesh was a fully unstructured mesh. To resolve near wall regions, Pointwise's "T-Rex" feature was used. The wall spacing was set to be 5×10^{-7} to ensure a $y^{+} < 1$ for the first cell off of the wall. This same spacing was used at all geometric changes. This included the spacing around the edges of the VGs. An additional line geometry was extruded from the tip of the VG. This allowed more control of the grid spacing off of the trailing edge of the VGs to better resolve the wake. The entire mesh included approximately 3.2 million cells.

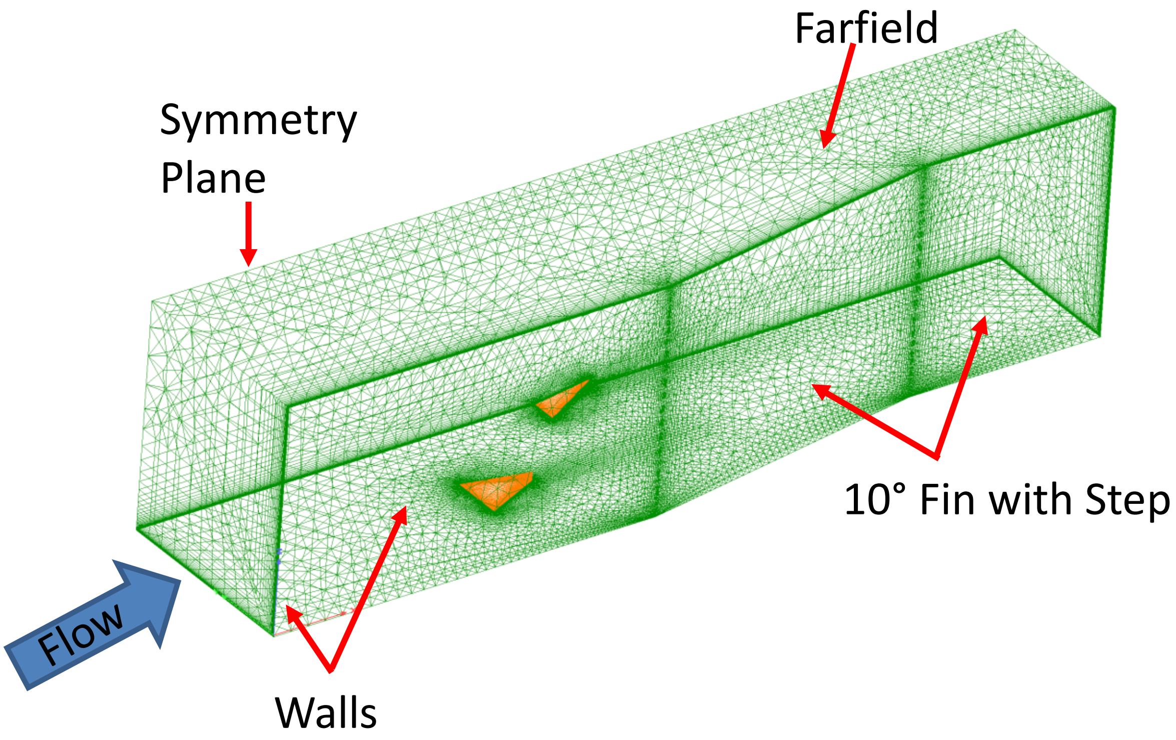

Figure 3.16 Surface mesh of the Mach 2 doublefin configuration with VGs.

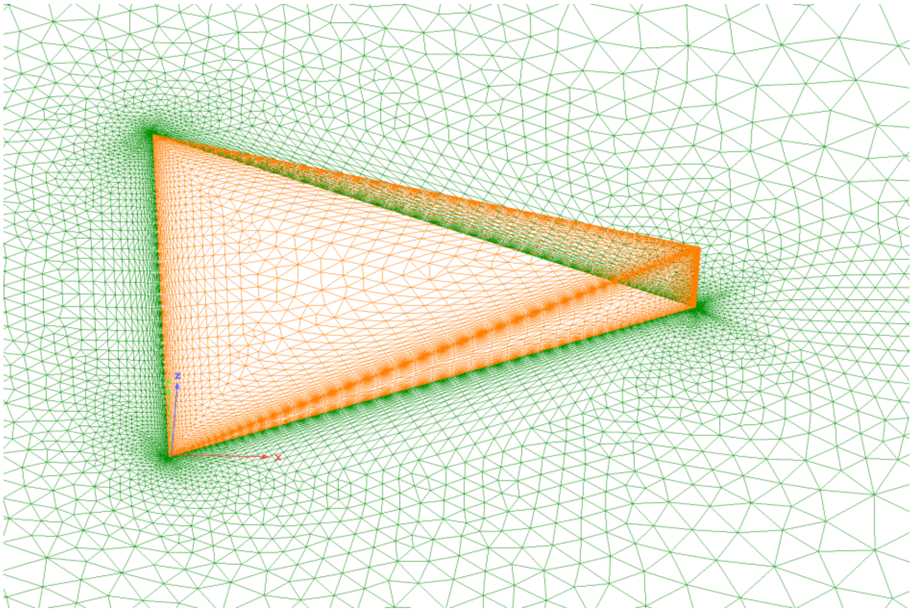

Figure 3.17 Zoomed view of VG surface mesh.

CHAPTER FOUR

RESULT AND DISCUSSION

4.1 Parameter Scaling on Mach 4.961 Interaction

Flow field nonuniformities are difficult to characterize in wind tunnels. To assist in the prediction of bulk flow distortion, the present study aims to quantify distortion sensitivities. Continuous scaling inputs of stagnation pressure, stagnation temperature, and wall thermal conditions were performed on a double-fin configuration at $M = 4.961$ to identify the dominant sensitivities to distortion. A calorically imperfect gas model was also studied as a categorical input since, at high Mach numbers, thermochemical effects may begin to impact the flow field. As such, inappropriate gas model selection may introduce unnecessary error and uncertainty.

One objective of this study was to determine uncertainties as they relate extrapolating ground tests to flight conditions. To achieve this, the conditions studied included the inflow conditions of existing ground facilities and cruise conditions a hypersonic vehicle may experience.

4.1.1 Turbulence Model Comparison

The results the Menter baseline and Menter SST models, were compared to existing experimental data. Figure 4.1 displays surface pressure extractions from the results of these two models compared to experimental data [60]. The figure displays normalized surface pressures in the spanwise direction at various streamwise locations. X=0 is the location of the fin leading edge. Figure 4.2 displays surface pressure contours of the interaction with vertical red lines displaying the locations where the pressure profiles shown in Figure 4.1 were extracted.

Figure 4.2 involves the same pressure locations as displayed in Section 3.3.2. The first two locations are upstream of the shock-shock interaction, where the baseline model qualitatively matches the experiments to a better degree than the SST model. Section 3.3.2 described the exact differences and experimental

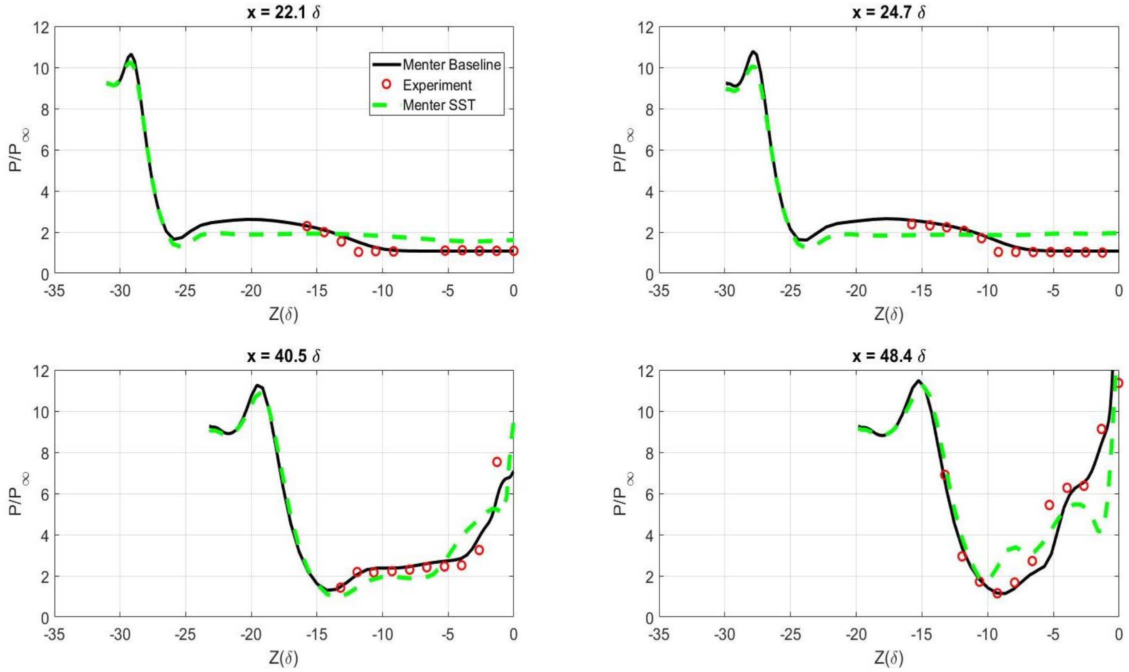

Figure 4.1 Comparison of surface pressures between Menter models and experimental data [60].

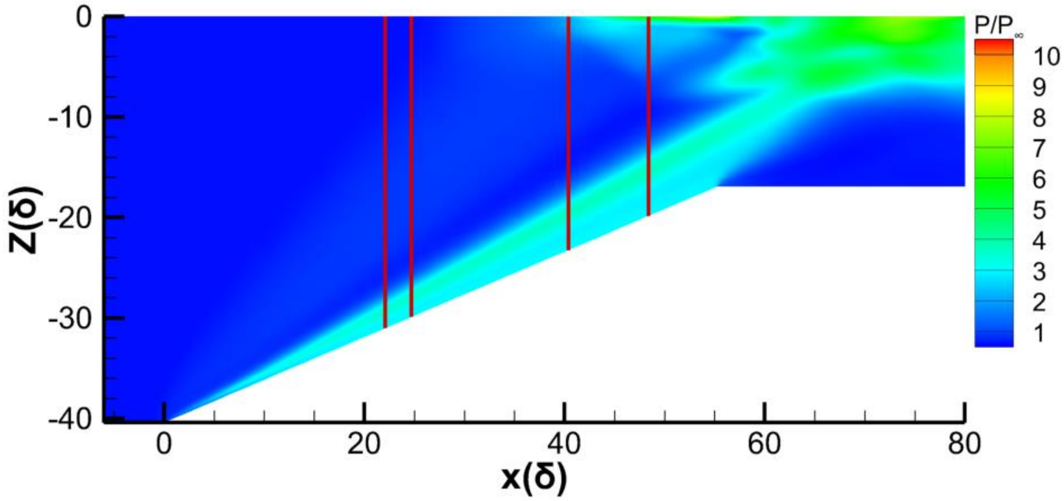

Figure 4.2 Surface pressure contours with extraction location lines.

uncertainty. The SST model matches the general trend; however, it smooths out the pressure distribution compared to the baseline model. It also over predicts the surface pressure, at nearly twice the ambient pressure. This is a result of the SST model predicting the upstream influence of the interaction further upstream than the baseline model. This caused the SST model to have a higher pressure at all extraction locations compared to the experimental results and the baseline model. Further upstream, the surface pressure for the SST case did match ambient conditions.

At $x = 40.5\delta$, effects of the shock-shock interaction are seen. The baseline model predicts these pressures well. The SST under predicts the shock location and does not match the experimental trend. At $x = 48.4\delta$, the baseline model begins to exhibit slight discrepancies with the experiments, with a mean absolute percentage difference of 6.6%; however, the general pressure trend still agrees. There is a slight shift in the pressure distribution, with the main disagreement being near the symmetry plane at $Z(\delta) = 0$. The SST model by comparison performs quite poorly. It also misrepresents the general trend of the pressure data. Based on the results of this comparison, the Menter baseline model was used for the rest of the cases.

4.1.2 Distortion Scaling

4.1.2.1 Test Matrix Justification and Definition

With a turbulence model selected, the scaling of this flowfield with Reynolds number and thermal conditions was studied. The independent variables that were scaled were Reynolds number and stagnation temperatures. Reynolds number was scaled by increasing stagnation pressure, as this is how most ground facilities vary Reynolds number. For static nozzles in unheated facilities, stagnation pressure is the only controllable flow variable. Three separate unit Reynolds numbers were selected, $Re = 60.0\times10^6$ m^{-1}, $Re = 36.5\times10^6$ m^{-1}, and $Re = 12.0\times10^6$ m^{-1} or $Re_\delta=228\times10^3$, $Re_\delta=138.6\times10^3$, and $Re_\delta=45.6\times10^3$ respectively based on the incoming boundary layer thickness. These Reynolds numbers were selected based on available ground facilities, test data, and flight conditions. $Re = 36.5\times10^6$ m^{-1} was selected as experimental and computational data currently exist for this geometry [15,60]. True flight Reynolds number was also a desirable data point. As such, $Re = 12.0\times10^6$ m^{-1} was included in the test matrix as this is the unit Reynolds number vehicles experience flying at $M = 5$ at an altitude of 60,000ft. This is a design altitude for the HIFiRE flight vehicles [66]. An appropriate, higher Reynolds number value was desired to complete the test matrix. A value of $Re = 60.0\times10^6$ m^{-1} was selected based on the Supersonic High-Reynolds (SHR) Tunnel from the National Aerothermochemistry and Hypersonics Laboratory based out of Texas A&M. This tunnel is capable of $M=5$ flow at this Reynolds number, and may accommodate similar geometries.

Beyond scaling stagnation pressure to vary Reynolds number, two separate stagnation temperatures were also studied at each of the three Reynolds numbers. There are large discrepancies between flight and ground stagnation temperatures, especially at high Mach numbers. One ground test facility compared in this study has a stagnation temperature of 427K [60], which is only roughly a third of the stagnation temperatures experienced in flight. At an altitude of 60,000 ft with an $M=5$, the corresponding stagnation and static temperatures are approximately 1280K and 217K respectively. The corresponding free stream temperatures are approximately 70K for ground tests (based on isentropic relations) compared to approximately 215K for flight conditions. Studying how these temperature differences affect the interaction is highly beneficial to the goal of the study.

Beyond simply scaling the stagnation temperatures of the flow, different wall thermal conditions were examined. The wall temperature can vary depending on the type of ground test. Short test time wind tunnel tests, such as a shock tunnel or a short-duration blowdown test, may experience nearly isothermal wall conditions. As the duration of the test time is short and the metal walls of a wind tunnel have a relatively large thermal mass, the walls may not noticeably change temperature throughout the duration of the run. By comparison, long duration wind tunnel tests, such as continuous tunnels or long duration blowdown facilities, may cool the wall significantly during the period of the run. If the temperatures of the wall and flow become similar, adiabatic wall conditions may be approached. Because of these thermal inconsistencies between various ground testing methods and flight conditions, wall thermal models were observed.

Understanding how the behavior of the flowfield varies with different wall thermal conditions may determine if the wall condition is a source of uncertainty. As such, adiabatic and temperature isothermal walls of 298 K were studied.

In addition to studying different wall thermal models, different gas thermal models were also observed. At such high Mach numbers, it was possible that the gas may not behave as an ideal gas. Past efforts concluded that local flow chemistry influenced shock structure, surface heat transfer, and pressures [67]. Imperfect behavior is more likely to occur at higher temperatures, and since wind tunnel tests are usually colder than flight conditions, an aim of the current study was to determine if a lack of these calorically imperfect effects in wind tunnel tests are a source of uncertainty. This gas thermal model study has implications for numerical work as well. Due to the increased computational expense of calorically imperfect models, it is common for simulations to use a perfect gas assumption. This assumption may not always be appropriate and could be a source of error for computational work as well. For this reason, the hottest flow temperature case of the current study was run with a calorically imperfect gas model to study its impact.

4.1.2.2 Quantities of Interest Justification and Definition

As this geometry represents a high-speed inlet, inlet performance metrics are the quantities of interest. A well-designed inlet attempts to maximize the amount of air captured while minimizing drag, pressure losses, and distortion. The current study proposes several metrics intended to represent these performance characteristics. These metrics were used as the system response quantities for the sensitivity study. The purpose of this sensitivity study is to determine which uncertain inputs dominate the system response.

Distortion was the primary observed metric as it is a good representation of the bulk flowfield that represents a departure from a well performing inlet [26]. It is ideal for a combustor to have as uniform a flow as possible, so understanding the non-uniformities that may be generated by the inlet may help the design process of combustors.

Quantifying distortion is a difficult task and consensus regarding its measurement has not been achieved [27,68]. Despite its difficulty to measure, qualitatively, distortion is clearly observable.

Figure 4.3 displays stagnation pressure at the outlet of the interaction. This view has mirrored the simulation across the symmetry plane to provide a better view of the full flowfield. The location of this extraction is 8δ downstream of the fin trailing edge, displayed in Figure 4.4. The purpose for extracting this plane so far downstream is to avoid capturing the immediate effects of the expansion generated by the geometry. As the geometry changed to a square duct after the fin trailing edge, the flow attempted to turn parallel to the wall. This expansion caused significant distortion located immediately at the fin trailing edge, which was quickly damped further downstream. As the combustor will likely be significantly far downstream as the immediate effects of this expansion will not be seen, the present study aimed to avoid studying a location with this strong influence.

Observing Figure 4.3, the non-uniformity of the flowfield is clearly seen. There is a region of significantly lower stagnation pressure near the symmetry plane created by the co-rotating vortices generated by the interaction. Corner effects generate a non-uniform distribution near the junction of the side wall and floor. Note, the top plane of this study was open, thus flow could freely escape from the top surface. The purpose for this study was not only to observe distortion, but to study how it changes at different conditions. Figure 4.5 displays the outlet at the same extraction location as shown in Figure 4.4. Both spatial dimensions shown in the image were normalized by the incoming boundary layer thickness, and the contours are of stagnation pressures. The difference between these three cases are different Reynolds numbers.

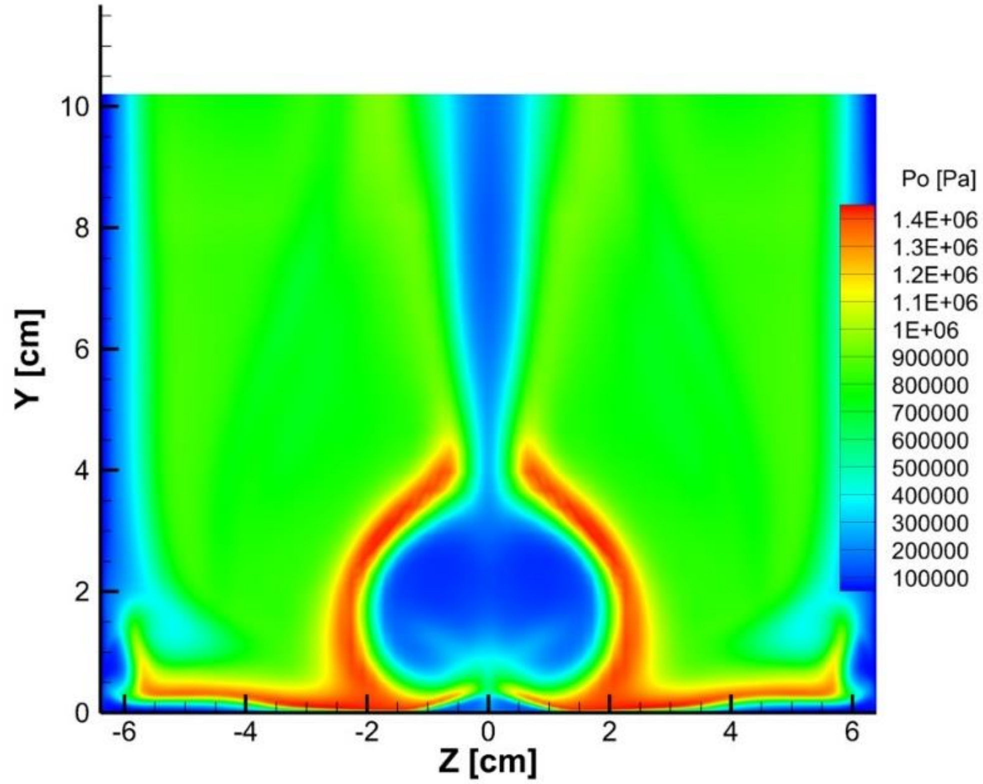

Figure 4.3 Outlet Stagnation pressure contours mirrored along the Z=0 plane.

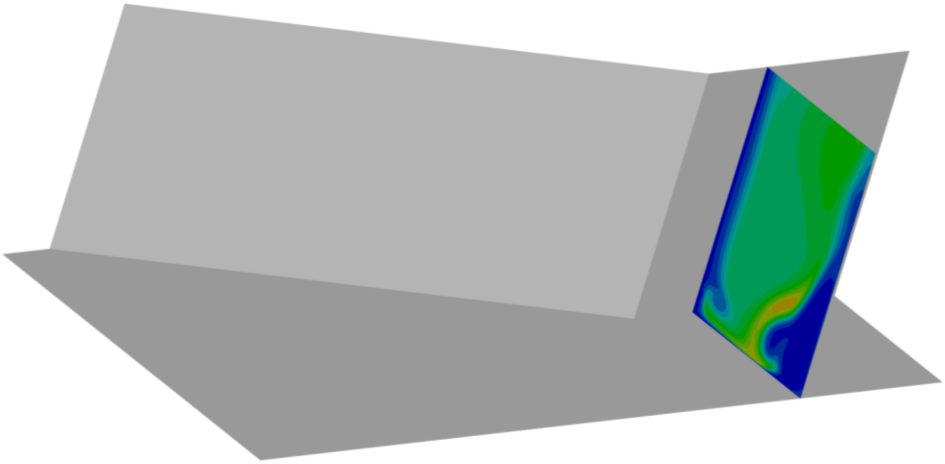

Figure 4.4 Outlet slice location with stagnation pressure contours.

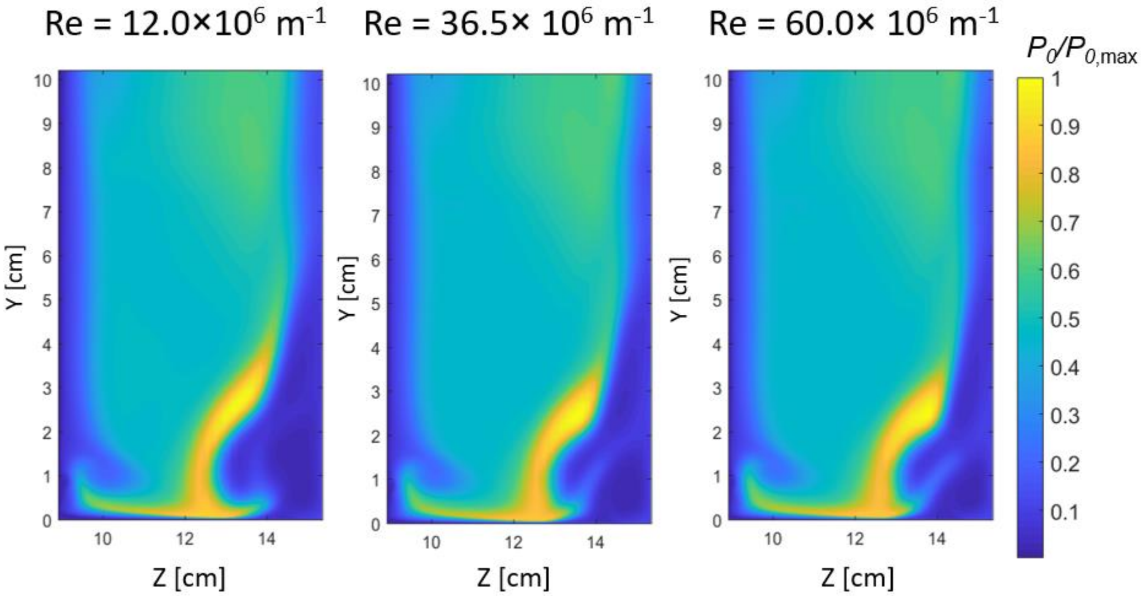

Figure 4.5 Outlet stagnation pressure countours normalized by maximum stagnation pressure at outlet.

The Reynolds number difference was created by scaling the stagnation pressure of the inflow while holding stagnation temperature constant at T_0 = 427K. To describe the distortion using a more quantitative method, the present study proposes three separate metrics: a distortion area (*DA*), a distortion width (*DW*), and a distortion coefficient (*DC*). The distortion area was intended to show the area of non-uniform flow. As this area was not a symmetric shape in all directions, the distortion width was meant to characterize the widest part of this distorted area. The distortion coefficient was created as a single metric to quantify the overall distortion levels at the outlet.

Distortion area was designed to determine the low stagnation pressure regions of the outlet, or the distortion bubble. To capture only the distortion bubble and not corner effects, only the half of the domain nearest to the symmetry plane was considered. The distortion area was determined by finding the maximum stagnation pressure gradient in the Z direction of the outlet. On each vertical plane, this maximum stagnation pressure gradient defined the left edge of the distorted region.

This is illustrated in Figure 4.6. The first image, Figure 4.6 (a.), in the figure shows the unaltered image of the outlet stagnation pressure contours normalized by the maximum stagnation pressure at the outlet. The dark portion in image Figure 4.6 (b.) is the calculated distortion area. Shown in image Figure 4.6 (c.) is distortion area overlaid on top of the original, unaltered image, Figure 4.6 (a.), to demonstrate exactly how the method of calculating distortion area compares to the overall image.

Also displayed in Figure 4.6 is distortion width. Distortion width was simply defined as the widest part of the calculated distortion area with a height greater than the boundary layer thickness. This height exclusion was performed since there was always lower stagnation pressure in the boundary layer. Since the goal was to capture the width of the distortion bubble, the boundary layer region needed to be disregarded, or the method would define distortion width to be within the boundary layer each time. Figure 4.6 (b.) illustrates distortion width.

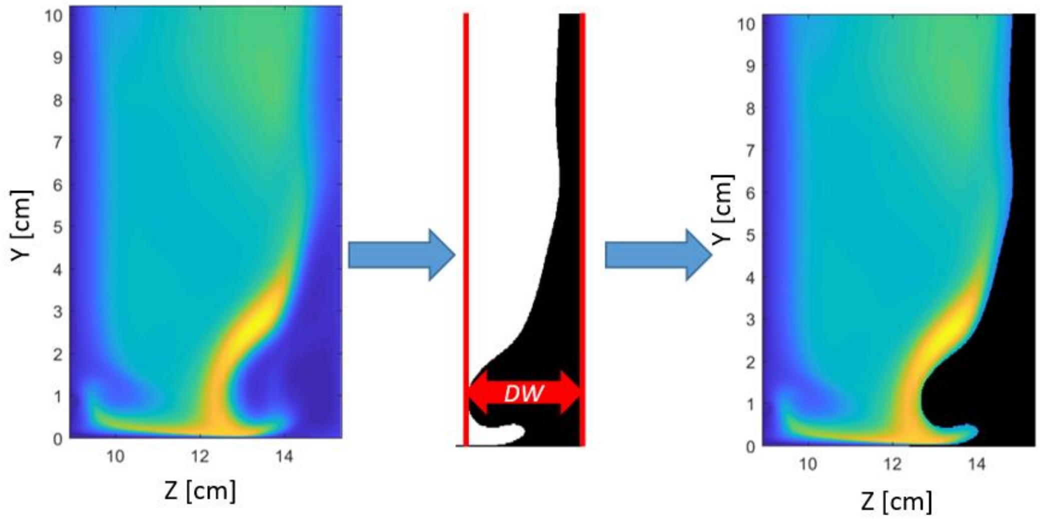

Figure 4.6 Distortion width and area illustration. (a). is the unaltered image, (b). is the extracted distortion area with labeled distortion width, and (c). is the distortion area overlayed on the original image.

The distortion coefficient was defined as the difference in average stagnation pressures of the outlet at different regions normalized by the maximum stagnation pressure of the outlet. This equation is shown in equation (4-1) where $\bar{P}_{02}$ represents the average outlet stagnation pressure and $\bar{P}_{02\theta min}$ represents the average stagnation pressure in the quadrant where stagnation pressure was at a minimum.

$$DC = \frac{\bar{P}_{02} - \bar{P}_{02\theta min}}{\bar{P}_{02}} \qquad (4\text{-}1)$$

Another quantity of interest was the difference in momentum flux between the inlet and outlet. Since momentum losses are ideally minimized in an inlet, understanding how this variable changed throughout the test matrix is another useful sensitivity study. This variable was simply calculated by summing up the momenta over the area at the outlet and the inlet and finding the percent difference between the two. In inviscid simulations, these distortion features were not present. This suggests that the observed distortion bubbles are viscously dominated effects.

4.1.2.3 Results of Distortion Scaling

All outlet distortion measurements were taken in the plane 8δ downstream of the fin trailing edge. Figure 4.7 displays the distortion area outlines of each of the cases, generated by the procedure described in the previous section. An example of each distortion width is also shown in the second frame of the image. The results of the three, distortion metrics described in the previous section, namely distortion area, distortion width, and distortion coefficient, are shown in the following tables.

Table 1 shows distortion width as a percentage of the total width of the domain. Note that the total width of the domain is half of the full inlet, as this table only looks at the half-symmetry domain. A plot of these same distortion width

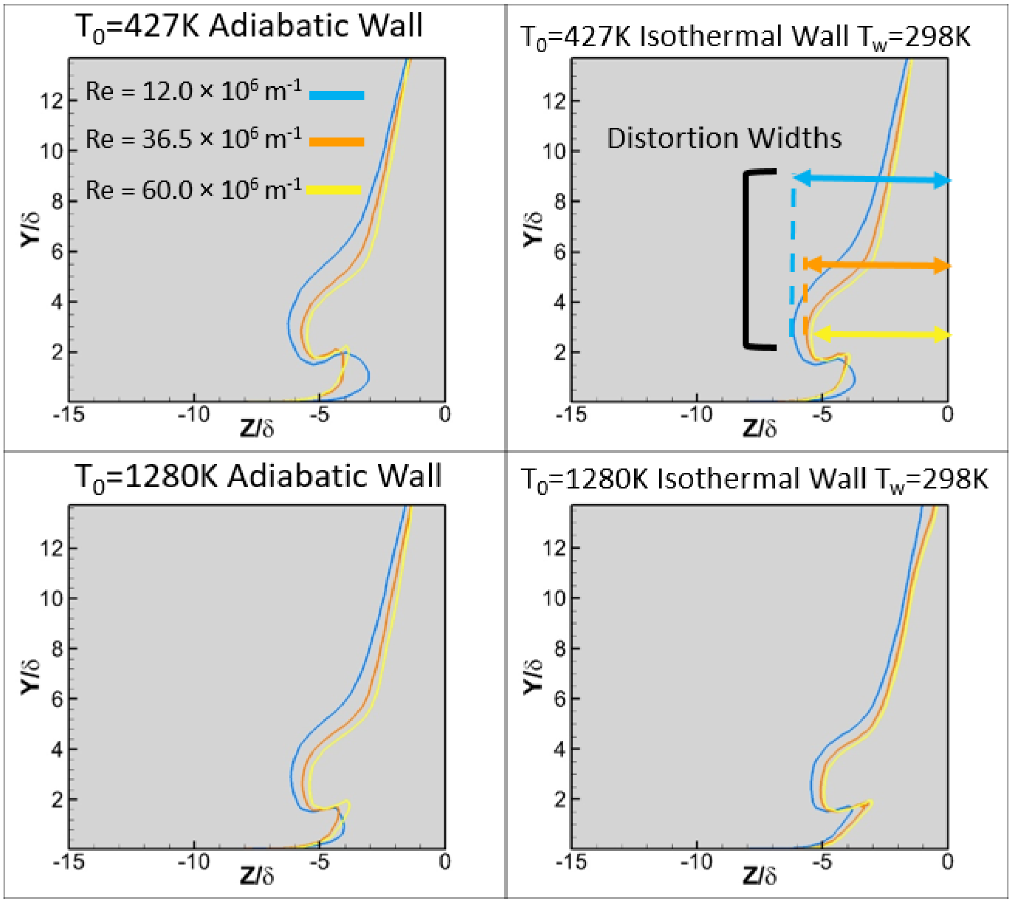

Figure 4.7 Distortion area outlines for each of the twelve cases.

Table 1. Distortion Width in Percentage of Total Width

Re/m	**12.0×10^6 m^{-1}**	**36.5×10^6 m^{-1}**	**60.0×10^6 m^{-1}**
Adiabatic Wall T_0=427K	37.12%	33.87%	32.71%
Adiabatic Wall T_0=1280K	36.19%	33.17%	31.79%
Isothermal Wall T_0=427K	36.00%	33.64%	31.79%
Isothermal Wall T_0=1280K	32.27%	29.93%	29.23%

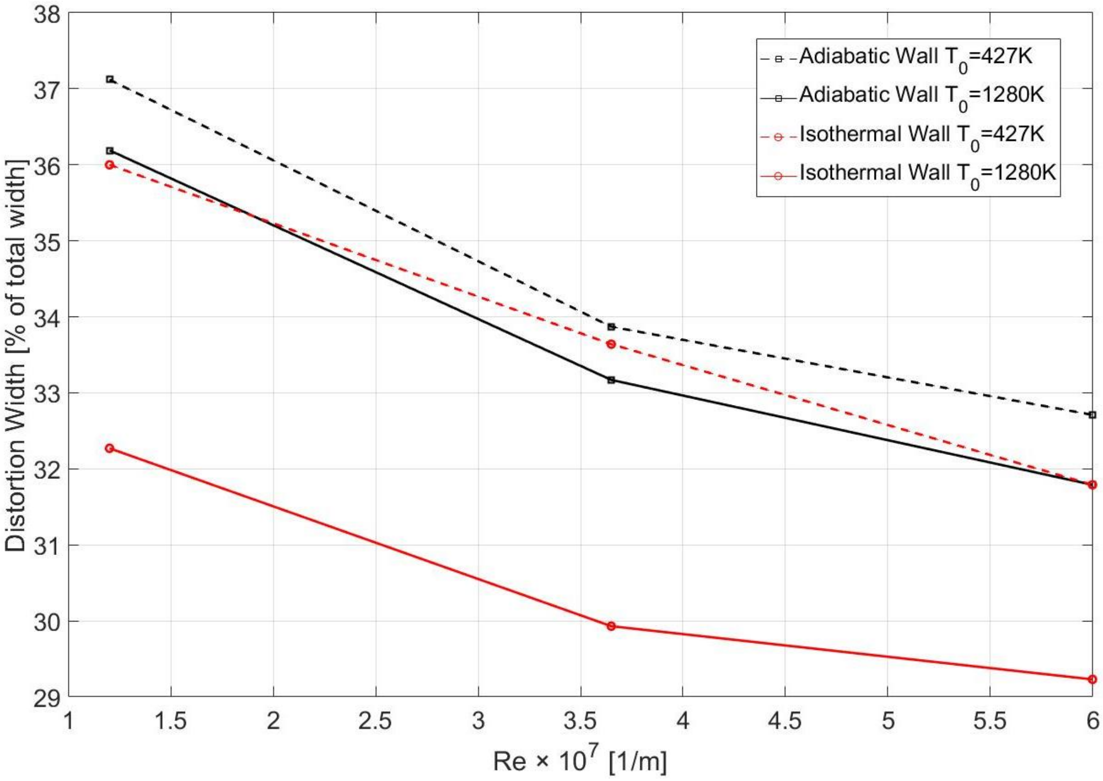

Figure 4.8. Distortion width against unit Reynolds number for each for each of the four cases. Isothermal wall temperature was set to 298K for all isothermal cases.

Table 2. Distortion Area in Percentage of Total Outlet Area

Re/m	**12.0×10^6 m^{-1}**	**36.5×10^6 m^{-1}**	**60.0×10^6 m^{-1}**
Adiabatic Wall T_0=427K	15.26%	13.11%	12.77%
Adiabatic Wall T_0=1280K	14.70%	12.65%	12.41%
Isothermal Wall T_0=427K	14.13%	12.83%	11.39%
Isothermal Wall T_0=1280K	8.76%	8.41%	7.93%

percentages is plotted in Figure 4.8 for a better visual representation. Similarly, Table 2 shows distortion area in a percentage of total area. This table is plotted in Figure 4.9. Table 3 and Figure 4.10 display the distortion coefficient. Lines between data points were plotted as a visual aid, however it was recognized that not enough points were studied to definitively interpolate between them.

For both wall thermal conditions at each stagnation temperature, distortion decreases monotonically as *Re* is increased. For the T_0 = 427K case, the slope of this change is greater between the lesser two Reynolds numbers cases compared to the greater Reynolds numbers. In contrast, at the higher T_0 = 1280K, the slope is relatively consistent throughout each case.

Observing the data from the isothermal wall with T_0 =1280K, distortion dramatically decreases. This suggests that distortion is sensitive to temperature-related variables, but not solely bulk flow temperature. Also contributing to the claim that distortion is sensitive to temperature is that distortion consistently decreases with increasing stagnation temperature. This trend holds true for each Reynolds number. This difference is most significant between the two isothermal wall cases. Since an overall trend for distortion does not appear with Reynolds number alone and distortion appears to be sensitive to temperature, distortion was examined as a function of local static temperatures. First, the static temperature was observed upstream of the interaction within the undisturbed boundary layer. The location selected was along the symmetry plane at a wall normal distance δ and 10δ downstream of the fin leading edge (6.05 cm from the inflow). This location was selected since differences between each case begin to appear, but this location is still upstream of the interaction. Figure 4.11 displays the temperature profiles extracted at wall normal distance δ along the symmetry plane for each of the three adiabatic wall cases with T_0 =1280K. An extraction within the viscous region was selected to ensure that the wall thermal model affected the temperature results. If the inviscid region was observed, the temperature profiles would primarily depend upon stagnation temperature, and wall thermal model may not have significantly influenced the temperatures.

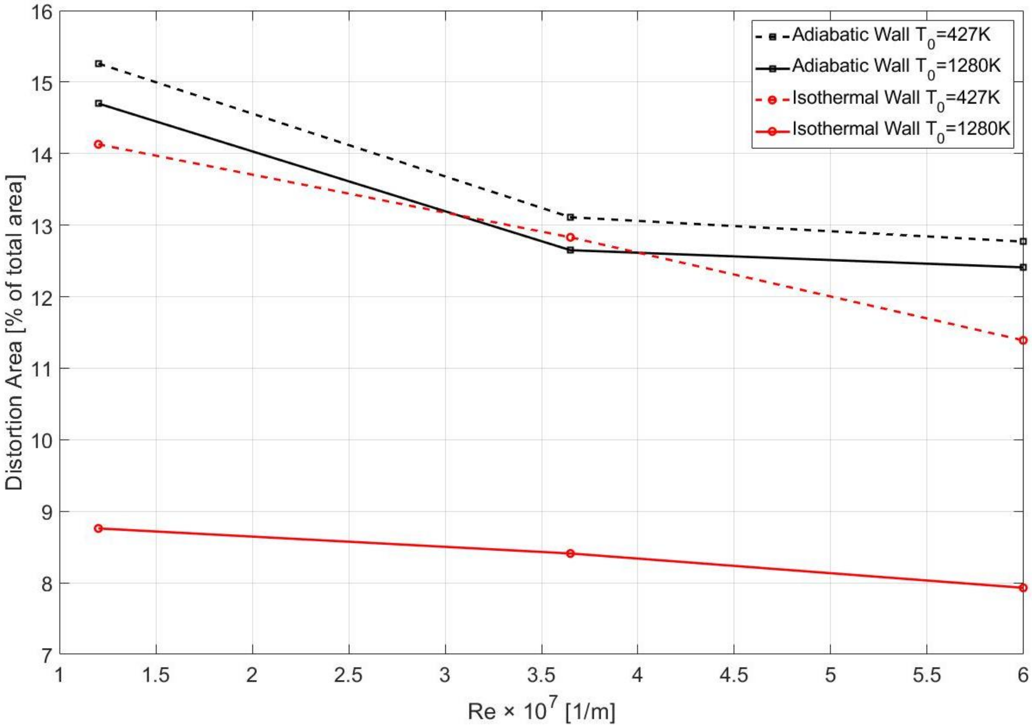

Figure 4.9 Distortion area against unit Reynolds number for each for each of the four cases. Isothermal wall temperature was set to 298K for all cases.

Table 3. Distortion Coefficient

Re/m	**12.0 × 10^6 m^{-1}**	**3.65 × 10^6 m^{-1}**	**60.0 × 10^6 m^{-1}**
Adiabatic Wall T_0=427K	0.752	0.729	0.724
Adiabatic Wall T_0=1280K	0.746	0.726	0.722
Isothermal Wall T_0=427K	0.738	0.729	0.721
Isothermal Wall T_0=1280K	0.706	0.671	0.656

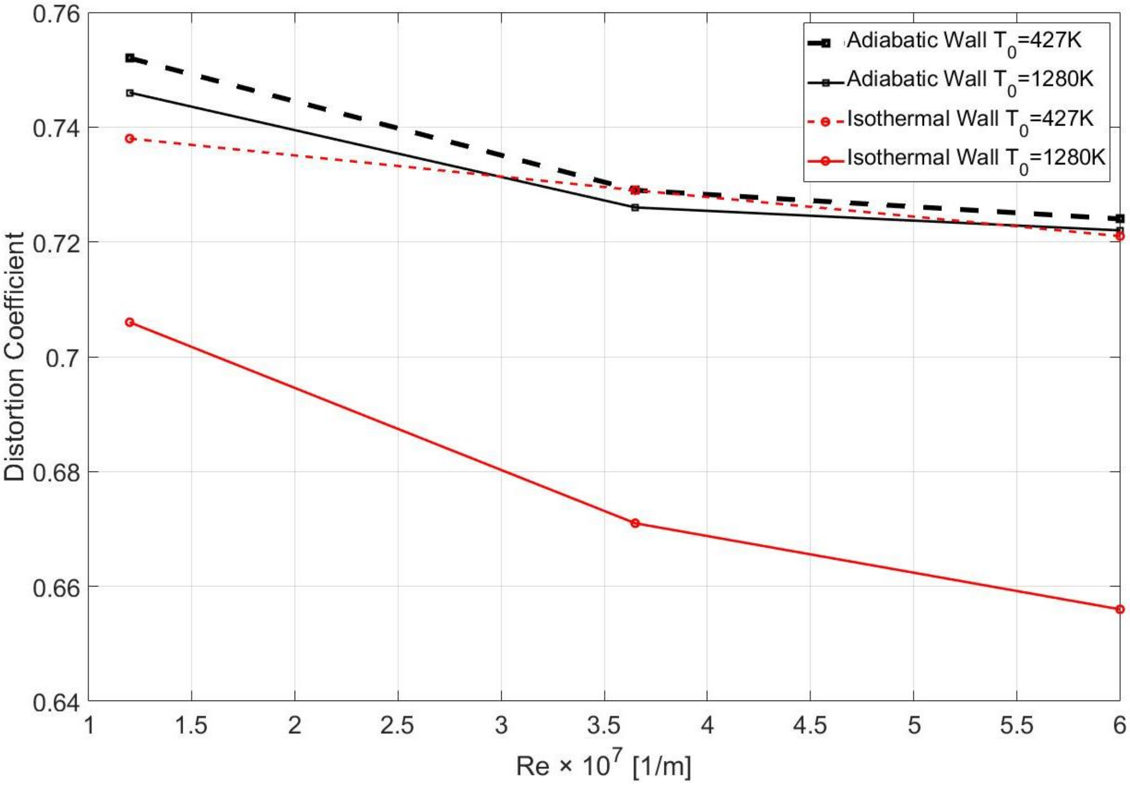

Figure 4.10 Distortion coefficient against unit Reynolds number for each for each of the four cases. Isothermal wall temperature was set to 298K for all cases.

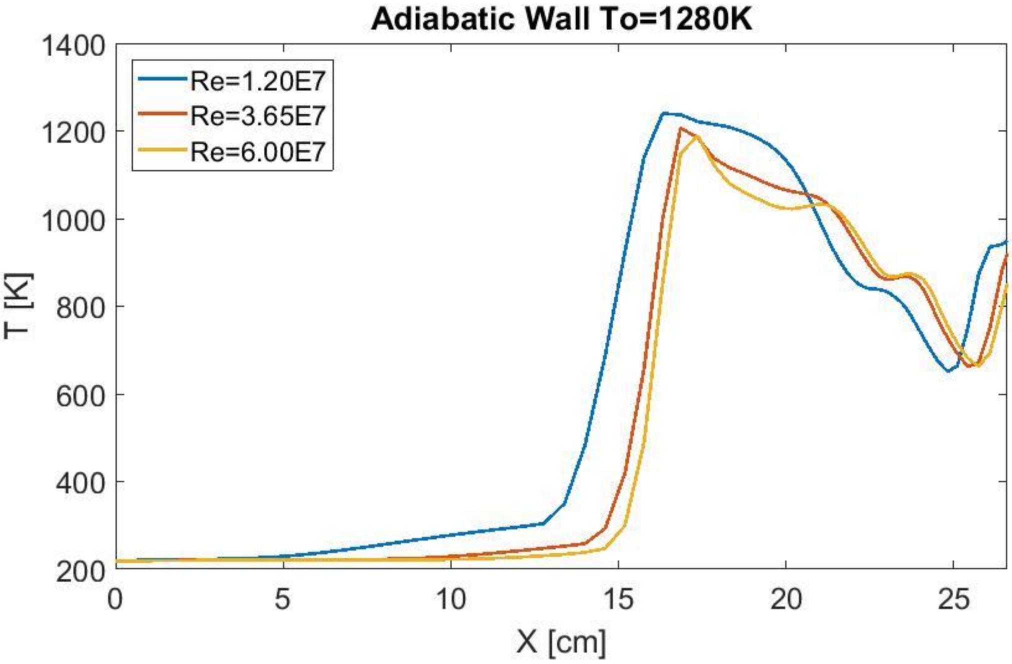

Figure 4.11 Static temperatures extracted at wall normal distance δ along the symmetry plane.

In Figure 4.11, the temperature can be seen to increase soon after the origin of the inflow profile. This temperature climb is due to the thermal boundary layer thickening. Within the inviscid region, static temperature is constant and equal between all three cases; however, thermal boundary layer growth directly affects the static temperatures of the studied region. Since this profile is extracted at a constant wall normal distance, differences in the thermal boundary layer height can cause the temperature to rise. This effect is illustrated in Figure 4.12 and Figure 4.13.

Figure 4.12 shows two separate thermal boundary layers extracted at the inflow and 5δ downstream of the inflow. Figure 4.13 plots these two temperature profiles normalized by the freestream temperature against the wall normal direction normalized by the boundary layer thickness. Note that this is the velocity boundary layer thickness and not the thermal boundary layer thickness. For turbulent boundary layers, this value is similar, however not identical [50]. The temperature is greater at the same wall normal distance for the profile further downstream. Therefore, the temperatures increase before the interaction in Figure 4.11.

After this initial, steady temperature increase, a sharp rise in temperature occurs due to the shock interaction. The temperature reaches its maximum within the separation bubble generated by the SBLI. The decrease in temperature after the structure is due to the flow reattaching as it is entrained in the co-rotating vortices seen in this interaction [22,69].

As Reynolds number increases, separation is delayed further downstream seen by the location of the temperature rise in each case. This is expected since a higher ratio of inertial to viscous effects should make the flow more resistant to separation. Besides differences in separation location and differences in temperatures, the overall behavior of all the profiles is the same.This is consistent for all twelve cases in the test matrix. The distortion coefficient was plotted against the temperature extracted at a consistent streamwise distance (10δ downstream of the fin leading edge, which was 6.05 cm from the inflow) for each case in Figure 4.14.

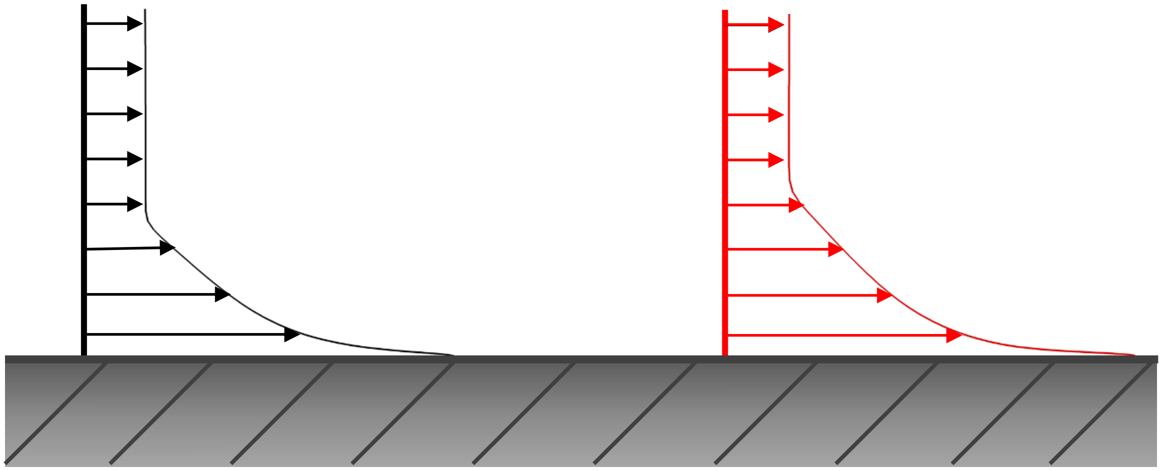

Figure 4.12 Thermal boundary layers at two separate streamwise locations.

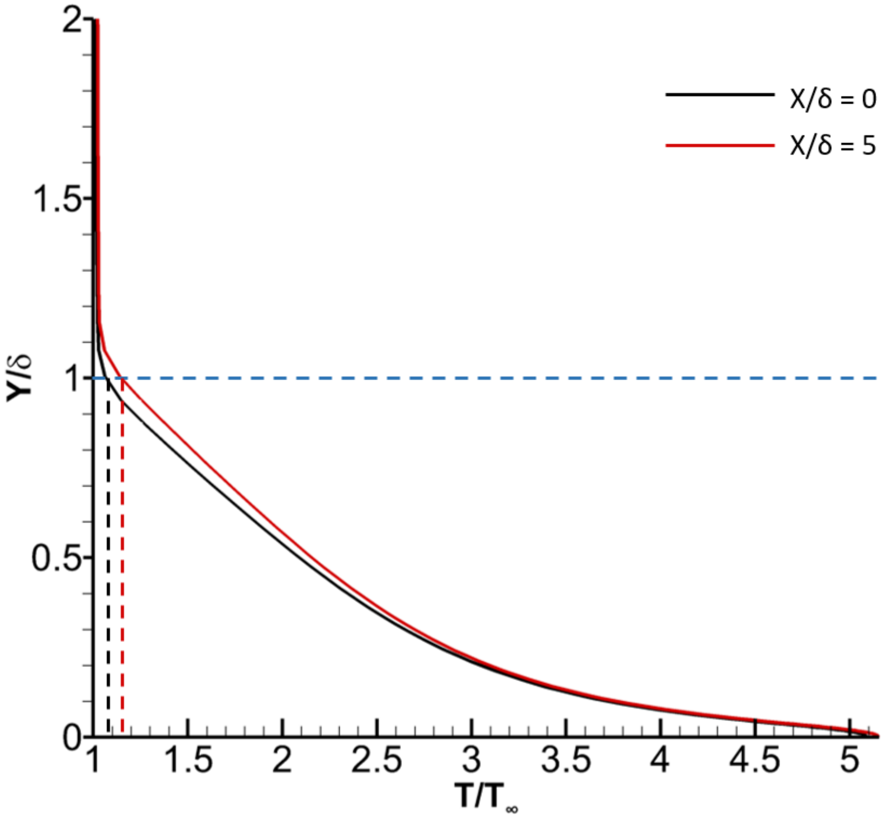

Figure 4.13 Thermal boundary layers at the inflow and 5δ downstream of the inflow.

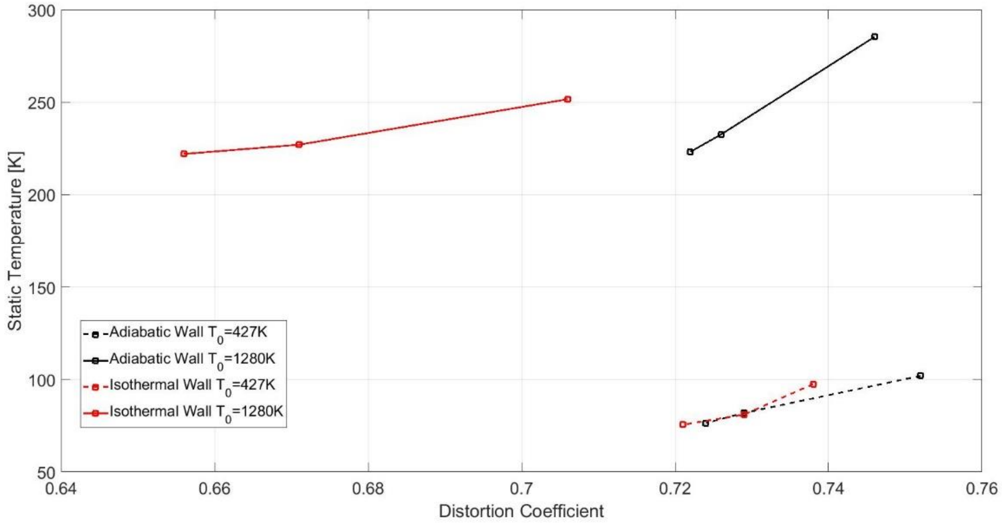

Figure 4.14 Distortion coefficient (eqn. 4-1) plotted against static temperature along the symmetry plane at a wall normal distance δ and 10*δ* downstream of the fin leading edge.

Throughout each case, distortion increases relatively linearly with increasing static temperature. This is consistent with results that determined a lower static temperature can reduce separation scale [8,70]. As static temperature is lowered, the subsonic portion of the boundary layer is thinner as the local speed of sound is lowered. Viscosity effects also decreases at lower temperatures, as defined by Sutherland's law resulting in a weaker SBLI at colder temperatures [70]. Since separation size impacts the total flow distortion, as static temperatures are lowered, separation and thus distortion is decreased. This suggests that wall temperature control may be an effective way to reduce distortion.

Although Figure 4.14 displays a consistent trend for each isolated case, finding a common trend across all cases would be beneficial. To find this, a different temperature extraction location was considered. For this case, temperature downstream of the interaction was examined. The temperature of the flow along the symmetry plane at wall normal distance δ was still studied, however instead of a constant downstream distance, a constant flow feature location was selected. The feature observed was the minimum temperature before the second compression. For clarity, this was located at approximately 24 cm downstream of the inflow for the $Re = 12.0\times10^6$ m^{-1} case referring to Figure 4.11.

A visualization of this feature is provided in Figure 4.15. This figure displays the T_0 =1280K and $Re = 12.0\times10^6$ m^{-1} case with static temperature contours normalized by the freestream temperature. The contours are displayed along the adiabatic wall and the symmetry plane. The purple dotted line in this figure represents where from which the temperatures in Figure 4.11 were extracted. The black dotted circle highlights the location of the temperature feature used for the next distortion study extraction. The bottom part of the figure displays an additional streamwise plane with static temperature contours and velocity vectors. This shows the movement of one of the co-rotating vortices generating this temperature feature.

Plotting the distortion coefficients for each case against the static temperature extracted from this feature results in the plot shown in Figure 4.16.

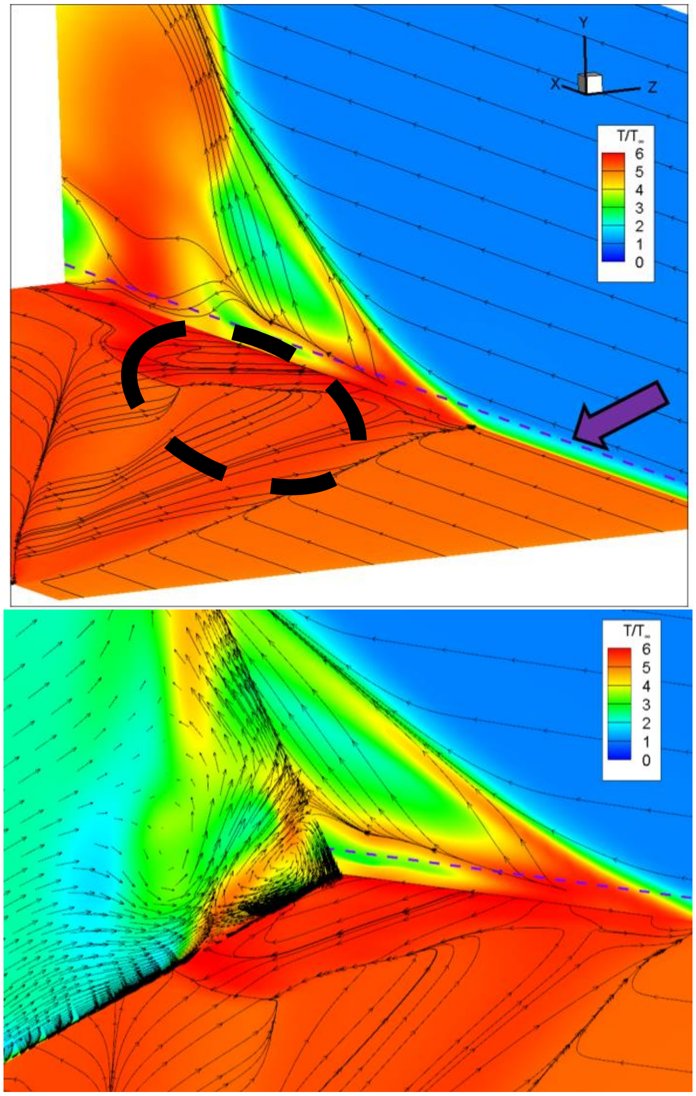

Figure 4.15 (top) Surface and symmetry plane temperature contours and velocity streamtraces where purple dotted line represents where static temperatures were extracted and black dotted circle highlights the temperature bubble generated by corotating vortices. (bottom) perpendicular plane included with velocity vectors.

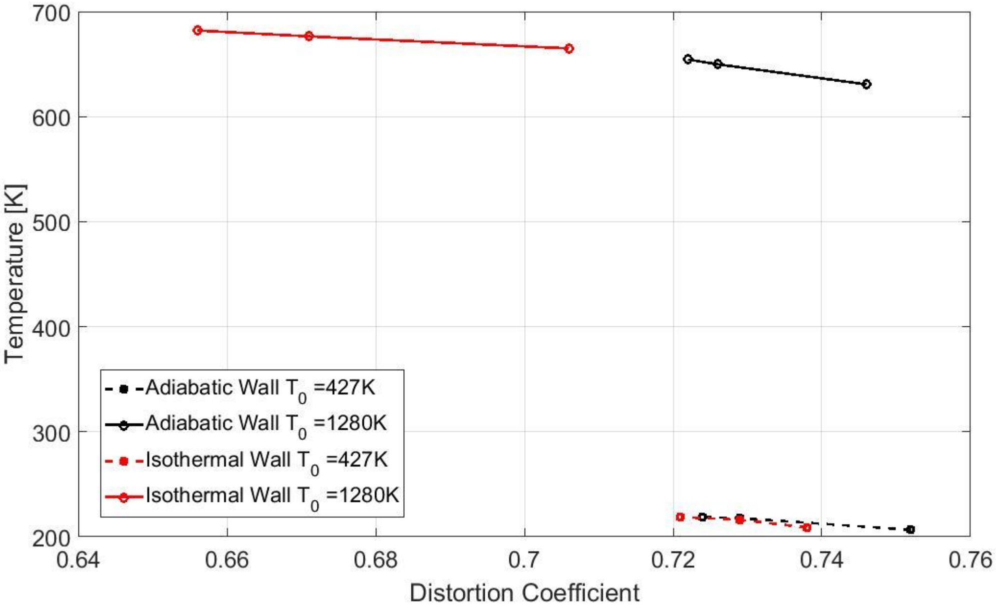

Figure 4.16 Distortion Coefficient plotted against minimum static temperature within co-rotating vortices along the symmetry plane at a wall normal distance δ.

The data collapses using this temperature extraction across all cases. At each stagnation temperature, a consistent trend can be seen among all Reynolds numbers and wall thermal conditions. For all the T_0 =1280K cases there was a calculated R^2 =0.935, and for all of the T_0 =427K cases, there was a calculated R^2 =0.924. Although this was only for three points, it had the best observable trend of the current study. This temperature could be a potential way to predict overall distortion levels with one data point. Interestingly, the trend is opposing that of the upstream extraction trend. Distortion and static temperatures have an inverse relationship at this location. Note, Figure 4.11 showed that the highest temperature going into the interaction had the lowest temperature at this extraction location. Due to this fact, it is expected that there would be an inverse trend looking at temperatures at this location. Wall cooling before the interaction paired with wall heating after the interaction may be a potential method to reduce overall distortion.

The effect of boundary layer health on distortion was also observed. Figure 4.17 plots the outlet distortion coefficient against the shape factor of the imposed inflow profiles for each adiabatic wall case. This factor was observed since either pressures or temperatures were being altered between each case. Since both variables affect density, they both will influence the boundary layer shape factor. All adiabatic wall cases show that an increased shape factor of the incoming boundary layer results in lower distortion. The isothermal wall cases did not collapse well onto the same plot. Since the isothermal wall resulted in sharp changes in temperature, and thus density, in the near wall region, the shape factors of these profiles were heavily affected.

Beyond observing general distortion trends, another question this work hoped to answer was how ground tests compare to flight conditions. It appears matching Reynolds number without matching stagnation temperatures introduces errors of varying degree depending on the case.

For the adiabatic wall cases, there were only very slight differences in distortion between the two different stagnation temperatures at a constant Reynolds number. The difference between the distortion widths and areas for the

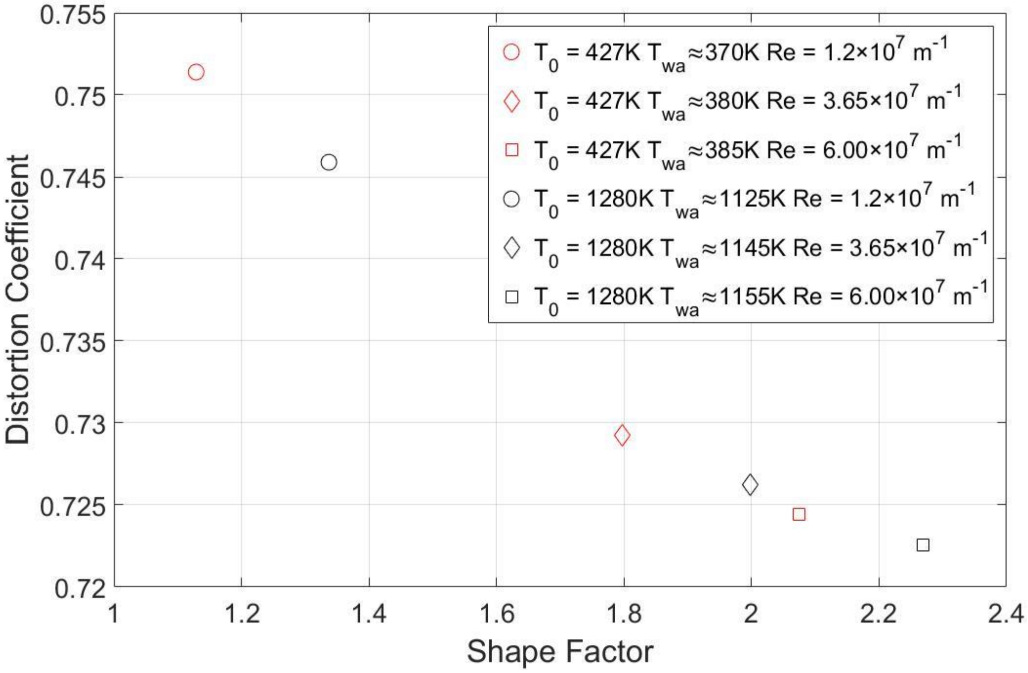

Figure 4.17 Distortion coefficient against incoming profile's shape factor for all adiabatic wall cases.

adiabatic walls at the two different stagnations temperatures for each Reynolds number were less than 1%. The difference in the distortion coefficients was less than 0.006 for each case. Although the difference is small for every case, for higher Reynolds number, the difference is at a minimum. This suggests that if Reynolds number is comparable for an adiabatic wall, matching stagnation temperatures does not introduce large errors in distortion. This is especially true for high Reynolds numbers.

This conclusion made for the adiabatic walls is very convenient; however, the trend for isothermal walls is different. Very large differences between constant Reynolds numbers at separate stagnation temperatures were seen for the isothermal wall cases. Like the adiabatic wall cases, the lower Reynolds number case experienced the greatest difference. For $Re = 12.0\times10^6$, the difference between distortion areas and width for the two stagnation temperatures was approximately 6%, and the difference between the distortion coefficient was 0.032. The implications of this result was that for isothermal walls, matching stagnation temperature as well as matching Reynolds number is important. This likely is due to the fact that these parameters affect the gas temperature in the boundary layer, which directly affects the density. This alters the compressible shape factor of the incoming boundary layer, which appears to influence the amount of distortion generated by interaction.

Comparing the different thermal models at constant Reynolds numbers and constant stagnation temperatures showed that wall thermal models impact the overall distortion. At T_0=427K, the difference between the adiabatic and isothermal wall cases was small. There was only about a 1% difference in the distortion areas and widths for the lower Reynolds number cases, with this difference decreasing as Reynolds number increased. The difference was greater at a higher stagnation temperature. The difference in the distortion area was about 6% between the isothermal and adiabatic wall cases with a $Re = 12.0 \times 10^6$ and T_0 = 1280K. As with all the other comparisons, as Reynolds number was increased, matching temperatures appears to be less important.

Although there were noticeable differences between the high stagnation temperature, isothermal wall cases, these cases are the least likely to be seen physically. Even though normal flight conditions do experience this high stagnation temperature, flight times are long enough where wall temperatures will approach static temperatures of the surrounding flow. Once this condition is met, the wall behaves nearly adiabatically. For this reason, the cases that best represent flight conditions were the adiabatic wall cases where T_0 = 1280K. The cases with an isothermal wall and T_0 = 1280K will likely only be seen for a very short duration in a vehicles flight domain, and since the distortion is lowest here, this will most likely not be the condition that will unstart an inlet due to distortion. Thus, it is arguably not necessary to experimentally match based on the current data.

The data sets most representative of ground testing was the adiabatic wall (representing continuous tests) and the isothermal wall (representing short term tests) with T_0 = 427K. Fortunately, the differences between both of these case sets and the representative flight conditions were relatively small. Interestingly, the isothermal wall behaves slightly better than the adiabatic wall in prediction of flight distortion when comparing the flight like case to the isothermal wall cases at similar Reynolds number. Thus, short term testing may be a better indicator of flight distortion levels. Overall, the data suggests that extrapolating ground tests' distortion levels to flight conditions is a reasonable approximation with only about a 1% difference in distortion levels.

4.1.2.4 Calorically Imperfect Gas and Cold Wall Case Comparisons

There were two additional metrics tested that did not seem to have a significant impact on the overall flowfield. The first being the calorically imperfect gas case. This gas model was employed for the hottest test case in the matrix, specifically at a unit Reynolds number of 60.0×10^6 with a stagnation temperature of 1280K. Qualitatively, the difference between the two cases can be seen in Figure 4.18. For easy comparison, the figure shows one symmetry plane of each model. The left half of the image is the perfect gas model, while the right half shows the calorically imperfect gas case. Note, these two simulations were run separately and, the slices were joined together during post processing. The contours are stagnation pressure normalized by the maximum stagnation pressure of each respective slice. The difference in the maximum stagnation pressures was less than 2%.

There are only slight differences between the two cases. Studying the quantities of interest, there was no difference in distortion width within reasonable levels of accuracy. Distortion area of the calorically imperfect case was 12.44% of the total outlet area, being only slightly higher than the perfect case at 12.41% of the total outlet area. The distortion coefficient of each case was 0.722 and 0.743 for the perfect and calorically imperfect case respectively.

Since it was shown that colder temperatures reduce distortion, it is unsurprising that the ideal case has slightly lower distortion. The calorically imperfect gas has more ways to store energy than the ideal gas, so available thermal energy is comparatively lower.

A colder isothermal wall case was also studied. As many tunnel facilities have pieces exposed to open air, it is possible that the wall temperature may change depending on the atmospheric temperature. Since wall temperature may have an impact on a SBLI [9], its effects on potential tunnel operating conditions were studied. Realistically, tunnel wall temperatures will not vary significant amounts, so the present study selected a wall temperature of 273K to compare to the 298K wall.

The difference between these two cases were negligible. Figure 4.19 plots the hottest two cases with the two isothermal wall temperatures against each other. Like the other plots, these profiles were extracted at height δ along the symmetry plane. There were slight differences in temperature, but it was not enough to alter the distortion or momentum flux more than 3%.

4.1.2.5 Momentum Flux Scaling

Beyond looking at distortion characteristics, identification of losses in momentum was also considered. Another performance metric of high-speed inlets is the amount of momentum the flow loses throughout its flow path.

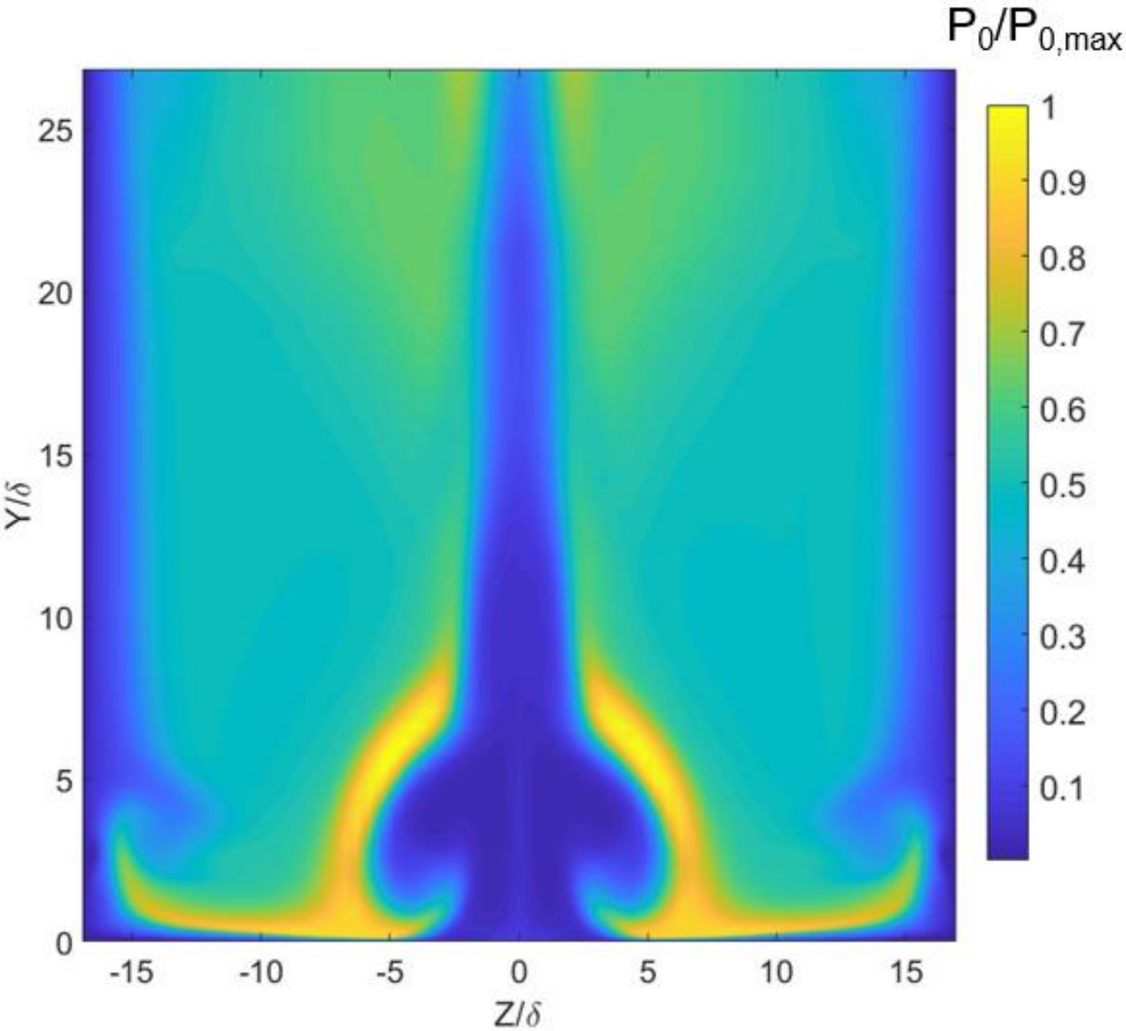

Figure 4.18 Normalized stagnation pressure contours for the perfect gas (left) and calorically imperfect gas (right) models.

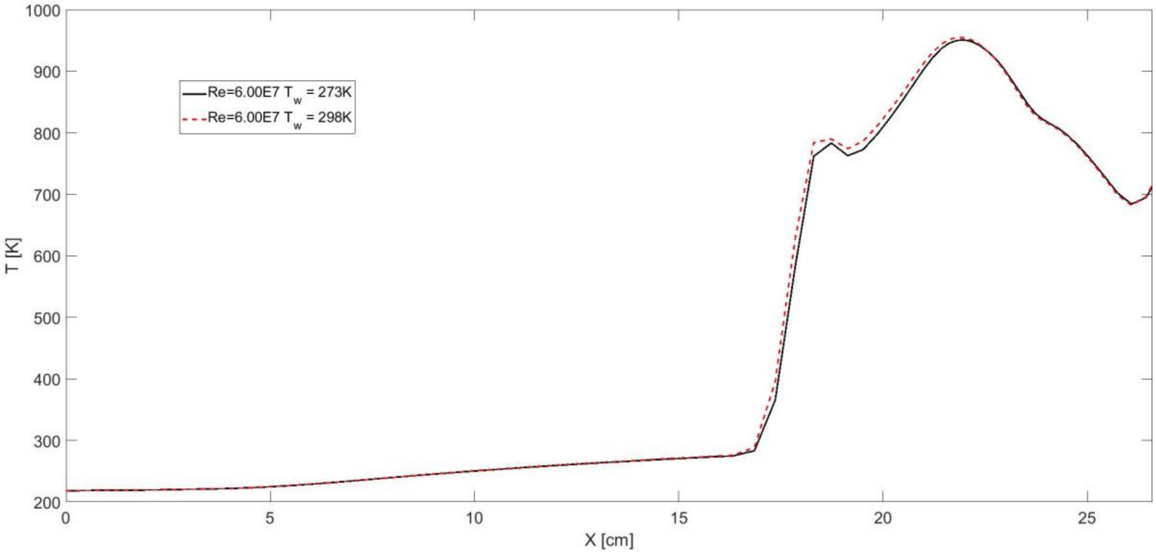

Figure 4.19 Isothermal Wall Temperature Comparison

The present study quantified this by calculating the momentum flux at the inflow condition compared to the extracted outlet. Figure 4.20 shows the difference between these two calculated quantities. The outlet plane was the same plane used for the distortion scaling study. To avoid any issues associated with an extraction at a boundary condition, the inflow plane for the momentum calculation was extracted 1δ downstream of the inflow condition. The momentum flux was determined by summing the momentum along the plane, calculated by multiplying density and the velocity magnitude, in both the inflow and outlet plane and dividing each summed momentum by their respective plane areas.

As previously mentioned, the top of this computational domain allowed flow to freely leave the boundary. Thus, there was momentum flux out of the studied volume that contributed to this momentum discrepancy between the inflow and outlet. To document this loss, the momentum flux leaving the domain through the top boundary is plotted in Figure 4.21. Since the inflow boundary condition was a one-dimensional profile, there was no flow exiting the top of the domain at this plane. Although the momentum exiting the domain is significant, it is three orders of magnitude less than the total discrepancy between the inflow and outlet planes, thus it does not invalidate any trends observed from Figure 4.20.

The most direct observable trend is that the momentum losses increase linearly with increased Reynolds number, with the slope of the change depending on stagnation temperature. Also, increasing stagnation temperature directly increases momentum loss. There is negligible difference between the isothermal and adiabatic wall cases when T_0 =427K. However, at T_0 =1280K, there is a noticeable change between the two wall models. This shows a similar trend to the distortion scaling study, where matching wall models is more important at higher stagnation temperatures.

Increasing Reynolds number produces an unsatisfactory result in momentum deficit. This trend directly opposes the ideal trend for distortion. The cases that exhibit lower distortion values correspond to higher momentum losses.

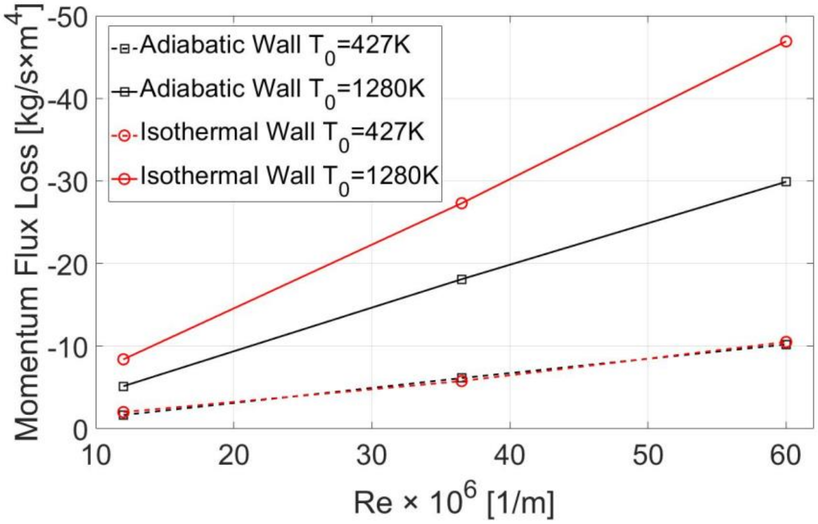

Figure 4.20 Momentum flux loss againt Reynolds number for each case.

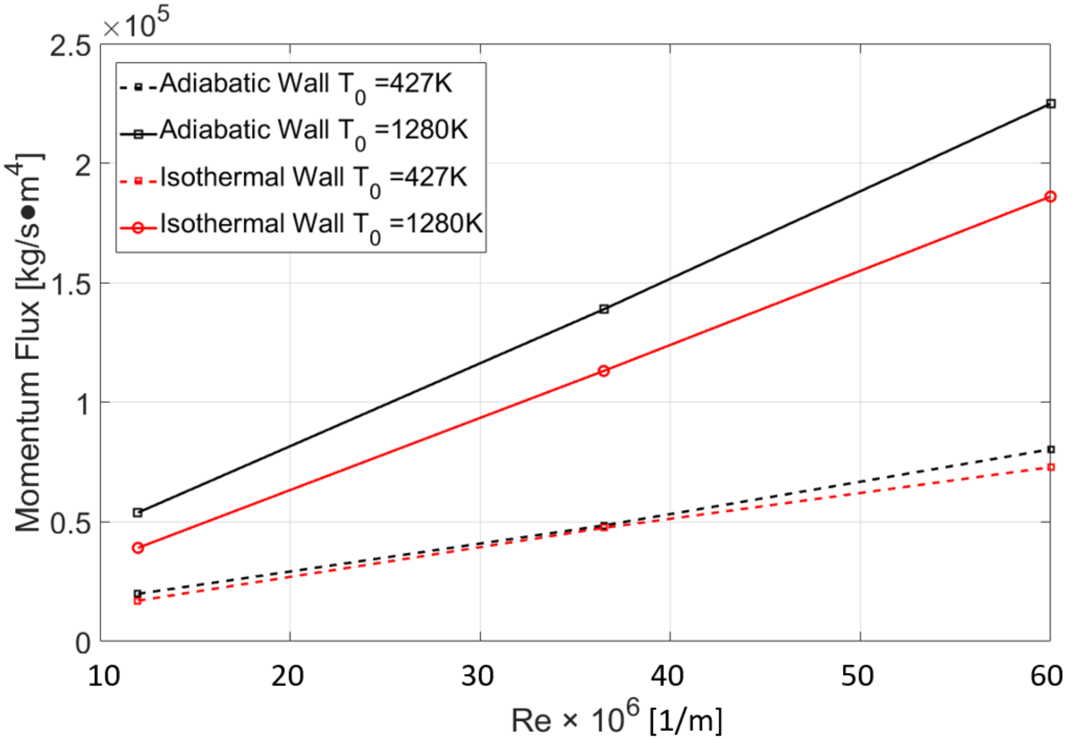

Figure 4.21 Momentum flux through the upper surface of the outflow plane.

The implication of this is that controlling and reducing distortion may negatively impact the efficiency of the inlet in the form of increased momentum losses. This introduces design conflicts, where a compromise may need to be made between ideal distortion and momentum efficiency.

4.2 Vortex Generators in Mach 2.01 Interaction

4.2.1 Experimental Campaign

Another goal of the current study was understanding the behavior of the double-fin interaction with passive flow control implementation. Vortex generators (VGs) were first studied experimentally in the Mach 2 blowdown facility. To determine their optimal placement with regards to delaying separation. Studies determining optimum vortex generator placements exist [39,49], though not specifically for this interaction. These previous studies focused primarily on an oblique shock wave interacting with a turbulent boundary layer as opposed to the crossing shock wave interaction of the current study. Also, limitations due to the size of the test section geometry of the facility used in this campaign prevented matching the configurations of the existing studies. The width of the test section, along with the proximity of the nozzle to the test section were the limiting geometric considerations for the experiments.

Initial experiments included a baseline case with no flow control, and a single VG along the centerline of the test section. Next, two additional VGs were placed such that their centerlines were 2 inches away from either another VG centerline or the tunnel walls. The streamwise placement was determined based on the distance away from the separation line of the baseline configuration, where x_s is the distance from the VG leading edge and the baseline separation line. This separation line was experimentally determined using oil flow on the baseline case. An example VG configuration is shown in Figure 4.22.

The maximum x_s was 4.75 inches, as this was the junction between the nozzle exit and the test section. The VGs were then moved downstream in one inch increments between runs until separation was no longer delayed further than

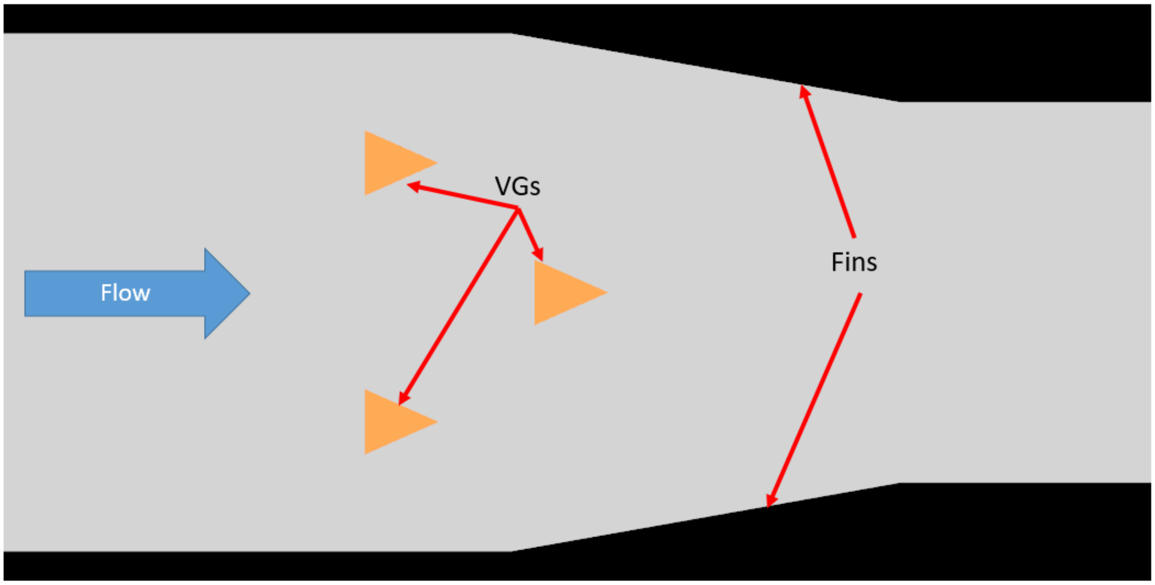

Figure 4.22 Vortex generator configuration in the Mach 2 tunnel

the baseline case. Figure 4.23 shows oil flow images of each case with a false color map applied using ImageJ, an open-source, Java-based image processing program.

The centerline separation location was determined experimentally by locating the intersection between the separation line of the single-fin interaction and a line drawn along the shock-shock interaction, parallel to the tunnel sidewalls. A visualization of these drawn lines is shown in Figure 4.24. Figure 4.25 displays the results of each of the experimentally determined centerline separation distances for each case where x/δ is the streamwise distance normalized by the boundary layer thickness and the fins leading edge is located at $x/\delta=0$. The single-VG configuration had two different cases. The original placement of the VG was slightly skewed, so this case was rerun after the positioning was corrected. It is still included in the figure as it shows proper alignment will delay separation further. Separation was delayed further downstream from the baseline case with the inclusion of the VGs for two of the three VG cases. At the VG placement furthest downstream, separation distance is no longer delayed past that of the baseline case.

The experimental results showed the capability of VGs in delaying separation distance. The best performing experimental VG configuration delayed separation distance by nearly 7% of the baseline case. It was found that the closest placement of VGs to the interaction can have detrimental effects. The case with the VGs closest to the interaction separated further upstream than the baseline case by 8%.

4.2.2 Computational Campaign

Mesh validation was performed before simulating the VG case that delayed separation the furthest downstream. Due to the geometry of the VGs, a fully structured mesh was not practical. The structured mesh had a mesh validation study performed on it for the steeper angle and higher Mach number simulated in the previous chapter.

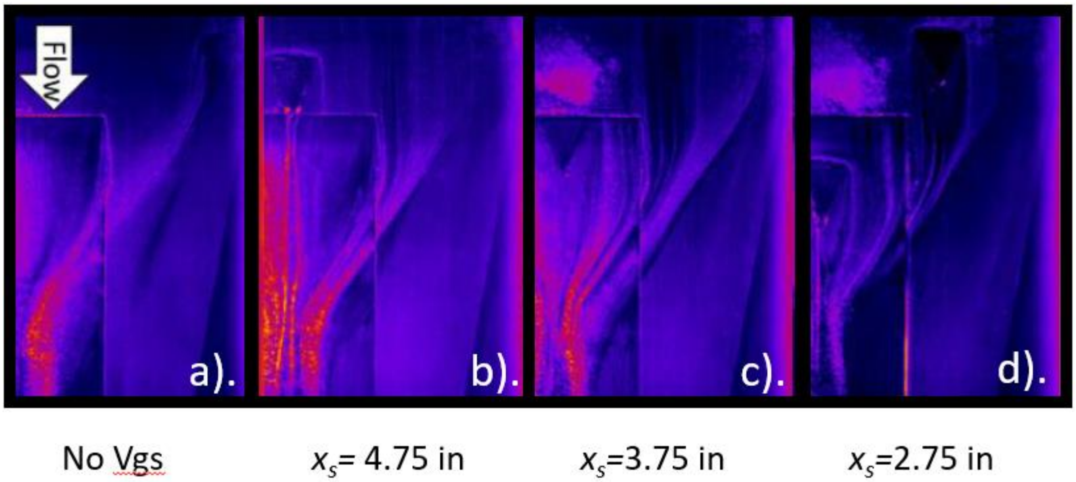

No Vgs x_s= 4.75 in x_s=3.75 in x_s=2.75 in

Figure 4.23 Oil flow comparison between the Mach 2 double fin configuration cases with the fins only and with VGs placed where x_s = 4.75, 3.75, and 2.75 inches for cases *a), b), c),* and *d)* respectively. Image courtesy of Katherine Stamper.

Figure 4.24 Visualization of how separation distance was determined.

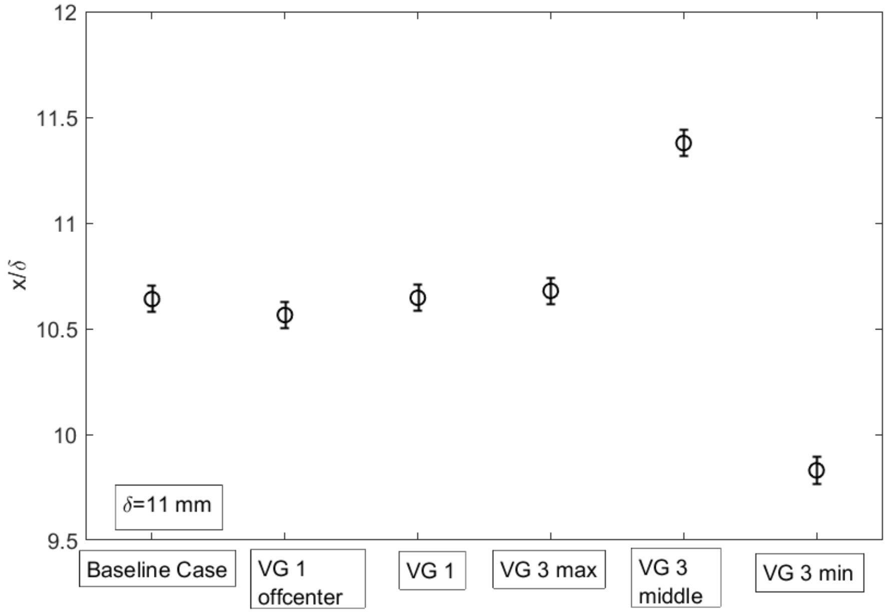

Figure 4.25 Separation distance from the leading edge of the fin normalized by boundary layer thickness. Experimental uncertainty was ± 0.1 *x/δ*.

To ensure that an unstructured mesh would achieve the same resolution, a structured grid and unstructured grid were generated for the same geometry. The structured grid was created with the same number of points as the M=4.961 case, with a y+<1. The unstructured grid was generated as described in Chapter 3, and was run without any VGs. The conditions of the simulations used the tunnel information and profile described prior in Section 3.3.3including a Mach number of 2.01, stagnation pressure of 240,000 Pa, and a stagnation temperature of 287K.

Since separation distance and stagnation pressure distortion at the outlet were the quantities of interest for this study, the skin friction coefficient (C_f) and the stagnation pressure at the outlet were compared between the two meshes. Figure 4.26 displays the skin friction coefficient plotted against the streamwise distance for the unstructured and structured grids at two separation spanwise locations. The two spanwise distances were 5δ and 10δ away from the side wall for each case.

Figure 4.27 displays the skin friction contours on the floors for each case, with red lines illustrating the extractions used for Figure 4.26. Note that in one half of each domain is displayed. The top and bottom halves of the figure are the unstructured and structured solutions respectively. The skin friction contours mostly agree between the two cases. There is a small discrepancy between the two meshes at $X/\delta \approx 10$ for the extraction at y=10δ from the side walls. This disagreement was likely caused by the mesh not aligning with shock, and at this streamwise location, the two shocks have collided.

There is a difference in minimum skin friction, however the minima occur at the same streamwise distance. As such, separation location does not differ noticeably between the two cases. Stagnation pressure of the outlet was also observed for the two cases. The outlet stagnation pressure contours are displayed in Figure 4.28 for both meshes. The unstructured solution is displayed on the left of the figure and the structured solution is displayed on the right. Extractions were performed in the wall normal direction at 0.2δ and 4δ away from the symmetry plane in the spanwise direction.

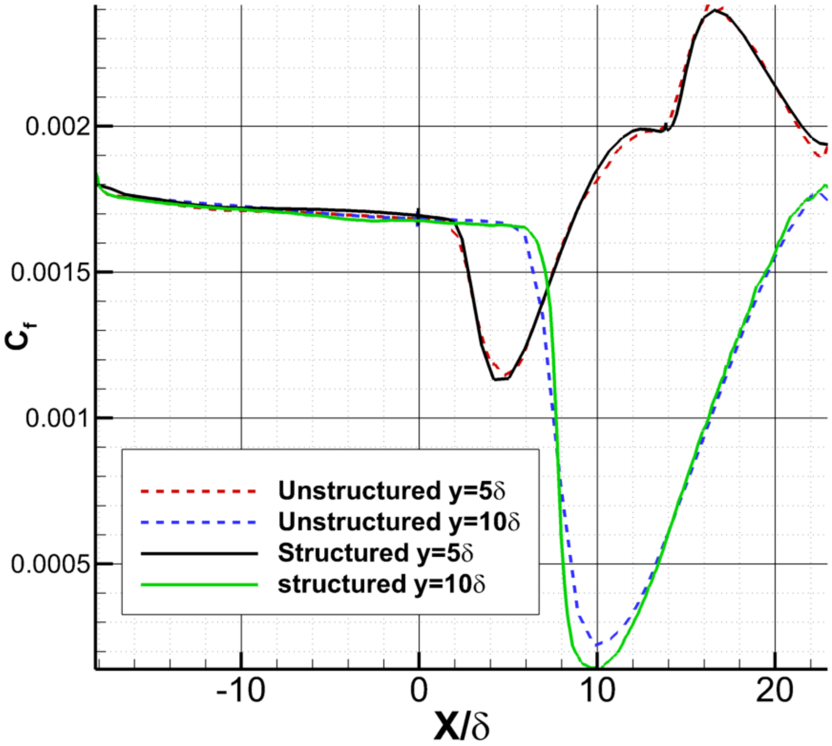

Figure 4.26 Skin friction coefficient plotted against streamwise distance for the unstructured and structured grids and two separate spanwise distances.

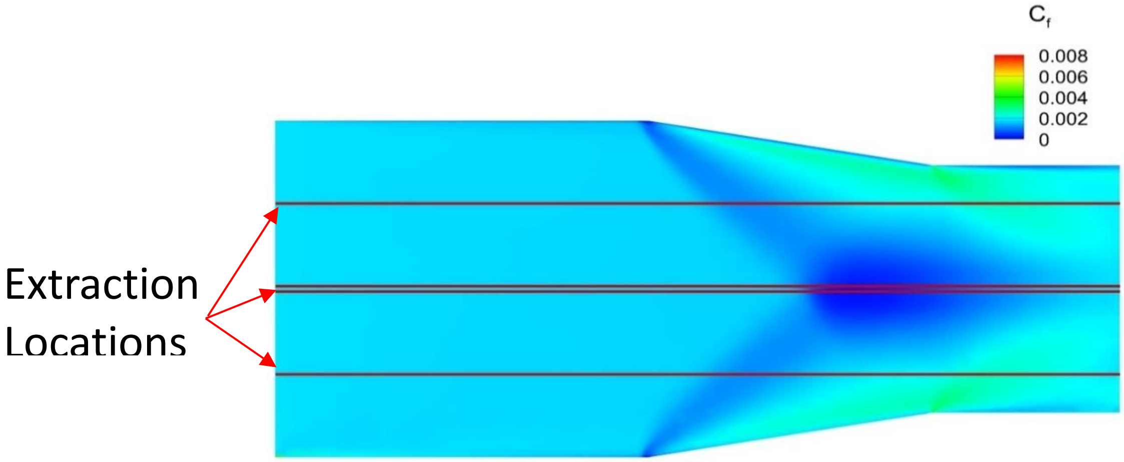

Figure 4.27 Skin friction coefficient contours with line extraction locations for the unstructured (top) and structured (bottom) grids.

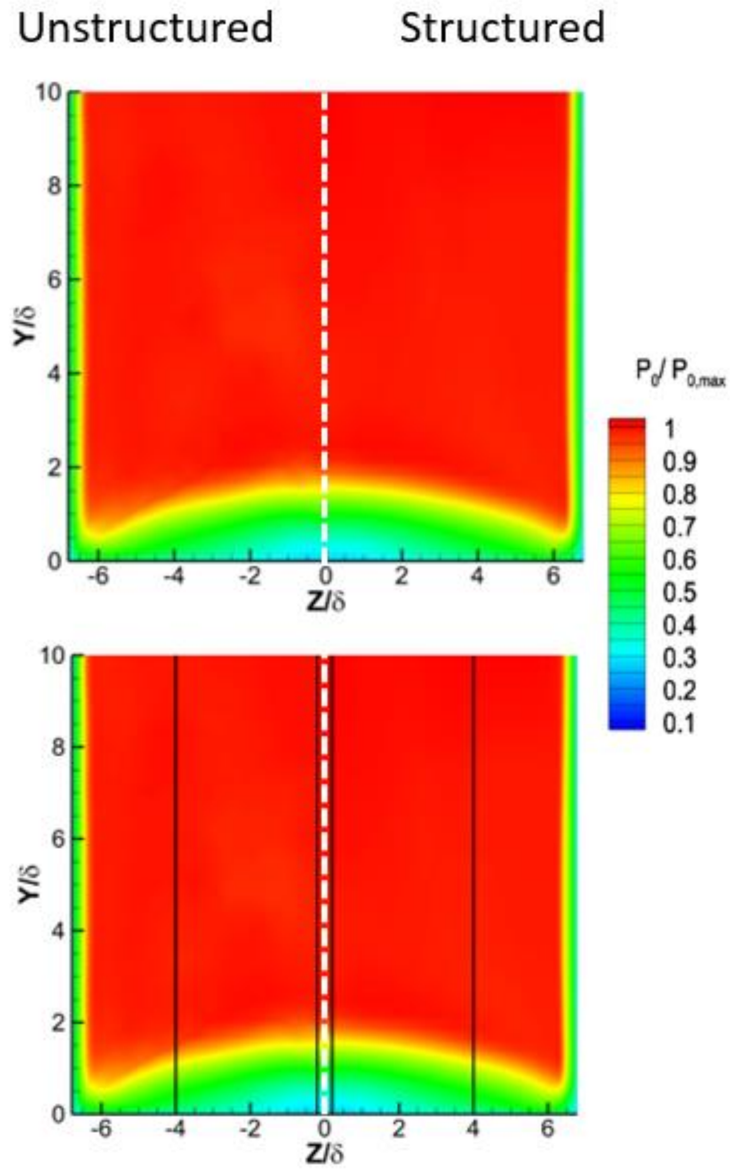

Figure 4.28 Stagnation pressure countours at the outlet for the unstructured (left) and structured (right) grids with extraction lines displayed on bottom figure.

The bottom image in the figure displays the extraction lines on the outlet. The stagnation pressures of this extraction are displayed in Figure 4.29. These extraction locations were selected as they are near where the VGs were placed in the later simulations. The contours of stagnation pressure between the two meshes are very similar. There is a slight difference between the boundary layer thicknesses near the symmetry plane, but overall, they are nearly identical. The stagnation pressure plots agree well for both extractions, however there are slight differences in the farfield. These differences never exceed 2%, thus the unstructured mesh appears to be properly resolved by this comparison.

The unstructured mesh was shown to model the interaction sufficiently, and viscous effects influence the interaction. The unstructured mesh with the addition of VGs, meshed as described in Chapter 3, was used to simulate the experimental case that delayed separation furthest. To validate the simulations, the experimental oil flow images were compared to numerical surface streamlines, shown in Figure 4.31 and Figure 4.32. The top images are the experimental oil flow and the bottom images are the computational surface streamlines. In both figures, the image shown on the right has a transparent oil flow image mirrored and overlaid on the computational streamlines for comparison.

The computational and experimental results are in excellent agreement for both cases. In the experimental image, a rectangular floor insert is seen. This is a permanent feature of the test section, and unfortunately slightly disrupts the oil flow. This causes a slight discrepancy between the simulations and experiments since the computational domain involves a perfectly flat, smooth surface. Despite the minor disagreement, the simulations reproduce the experimental mean flow features. For the case without VGs, determining separation the same way as was done experimentally results in a separation distance of $x/\delta = 10.5$, compared to the experimentally determined $x/\delta = 10.6$.

For the case with VGs, there is a slight difference in VG placement between the experimental and computational domains. Experimentally, the vortex generators were not placed exactly as designated. A slight misalignment between

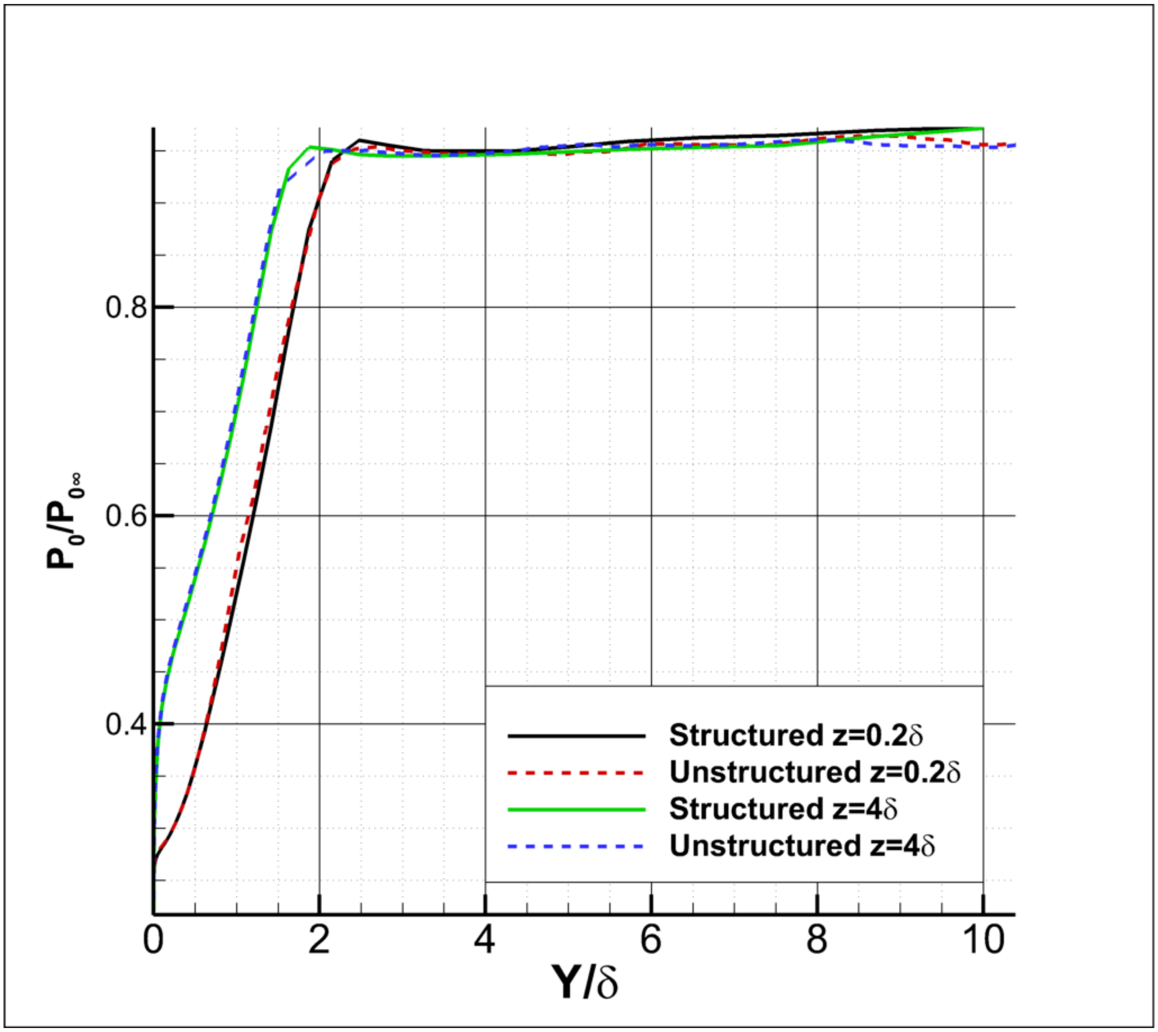

Figure 4.29 Stagnation pressures again wall normal distance for the unstructured and structured meshes.

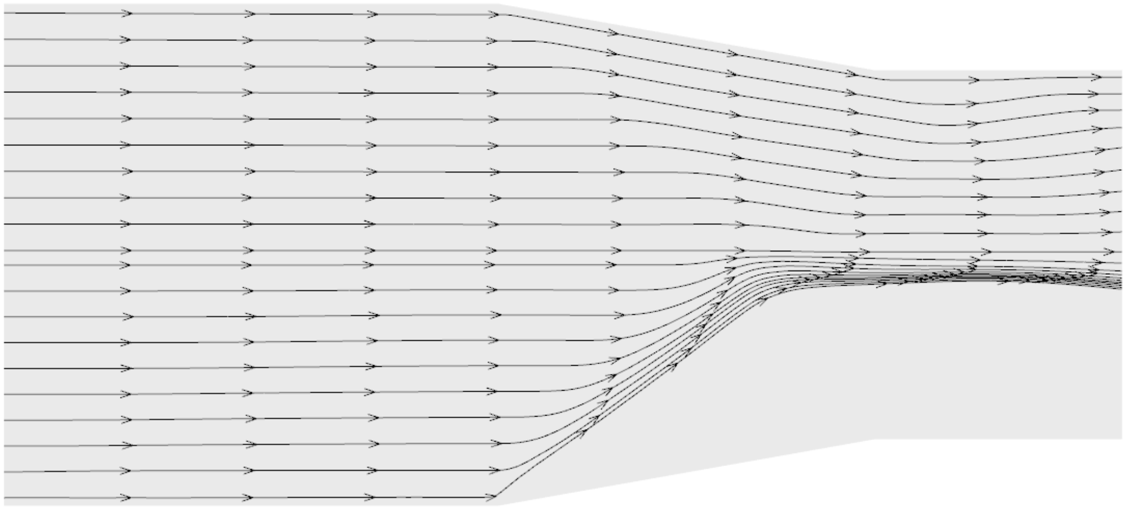

Figure 4.30 Invsicid (top) and viscous (bottom) surface streamtraces.

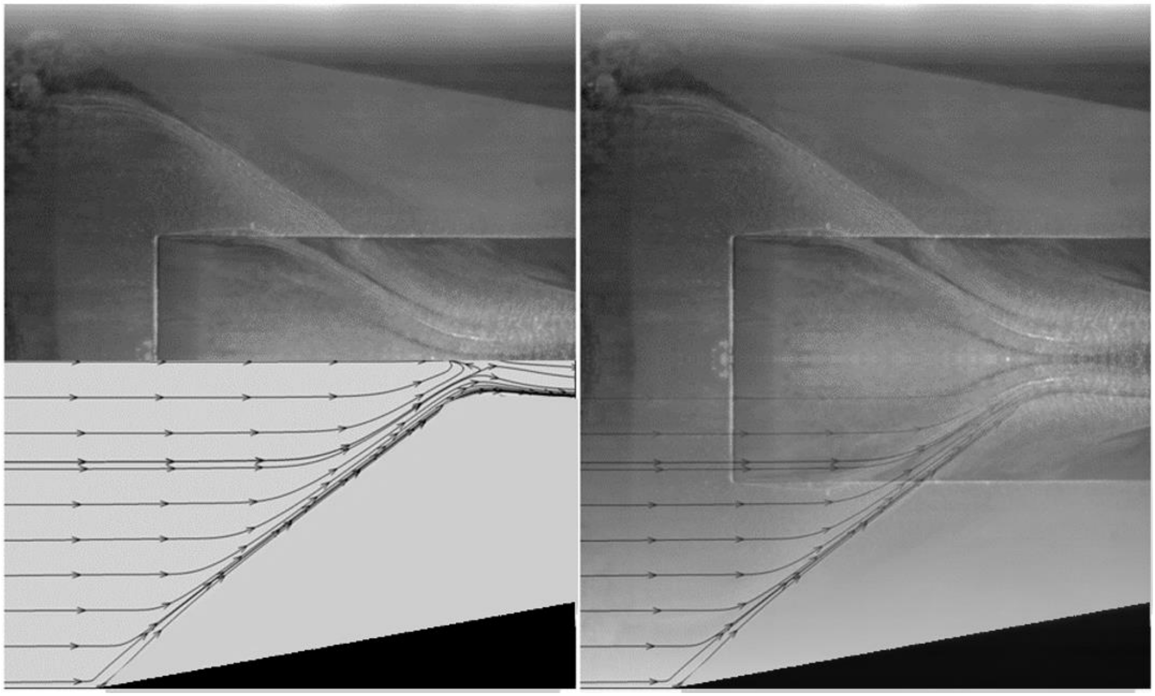

Figure 4.31 Experimental oilflow against computational streamlines for the baseline case.

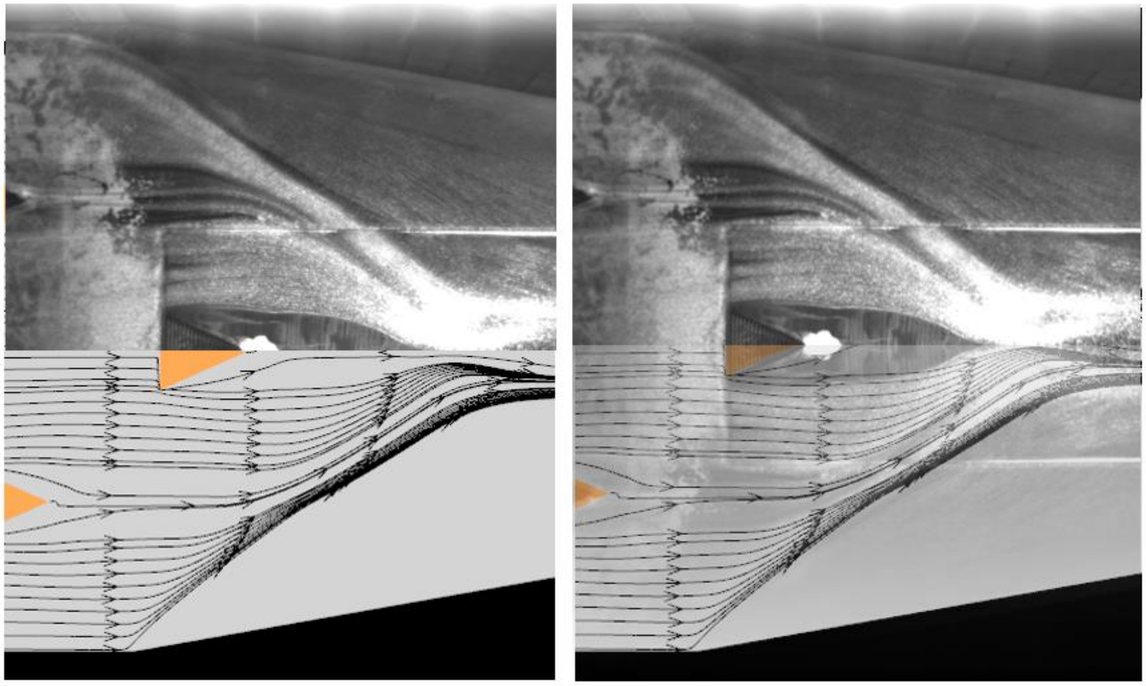

Figure 4.32 Experimental oilflow against computational streamlines for the VG case.

the upstream VGs as seen in Figure 4.32, though the offset is less than 0.25δ and is likely not significant. This offset can be seen by observing the upstream VG trailing edges. The overlaid experimental image VG is slightly further upstream than the computational VG. The mean features are still nearly identical between the two cases, again proving that the mean flow features are reproduced.The computational and experimental results both determined separation was x/δ = 11.4.The surface flow comparison shows that the simulations are able to properly model the mean flowfield. Since distortion is difficult to measure experimentally simulations can aid in the understanding of this phenomena. Many studies have shown that separation is delayed through the use of VGs [41,43,71], though few studies have focused primarily on how VGs effect overall flow distortion [41]. It can be hypothesized that the introduction of protuberances into the flowfield will induce additional non-uniformities into the flow field.

This is visualized in Figure 4.33. This figure displays a similar outlet plane as shown in the previous section. The contours in the image are stagnation pressures normalized by the maximum stagnation pressure of each outlet. A half symmetry display of each outlet is shown in the figure. Figure 4.33 is split at the centerline, where the case without the use of VGs is shown on the left and the case with the use of VGs is shown on the right.

There are losses in stagnation pressure as a direct consequence of the use of VGs. Large regions of lost pressure can be seen at the locations where the VGs were implemented, also introducing non-uniformities into the flowfield. Though the use of flow control did delay separation, it was not without a deficit.

This interaction was too weak to generate the distortion features seen in the M = 4.961 interaction, so the previously used distortion metrics do not apply well in this case. However, momentum deficit was calculated for this case. The use of VGs caused a 6.1% loss in total momentum at the outlet compared to the baseline case. Momentum was calculated identically to how it was calculated in the previous section. Like the previous domains, the top boundary for these cases do allow air to exit the domain through the top surface. The case with VGs has 2.4% higher momentum flux leaving the top boundary of the domain. Like the results of the distortion scaling study, effectively controlling the influence of the interaction has an impact on the efficiency of the inlet in terms of momentum losses.

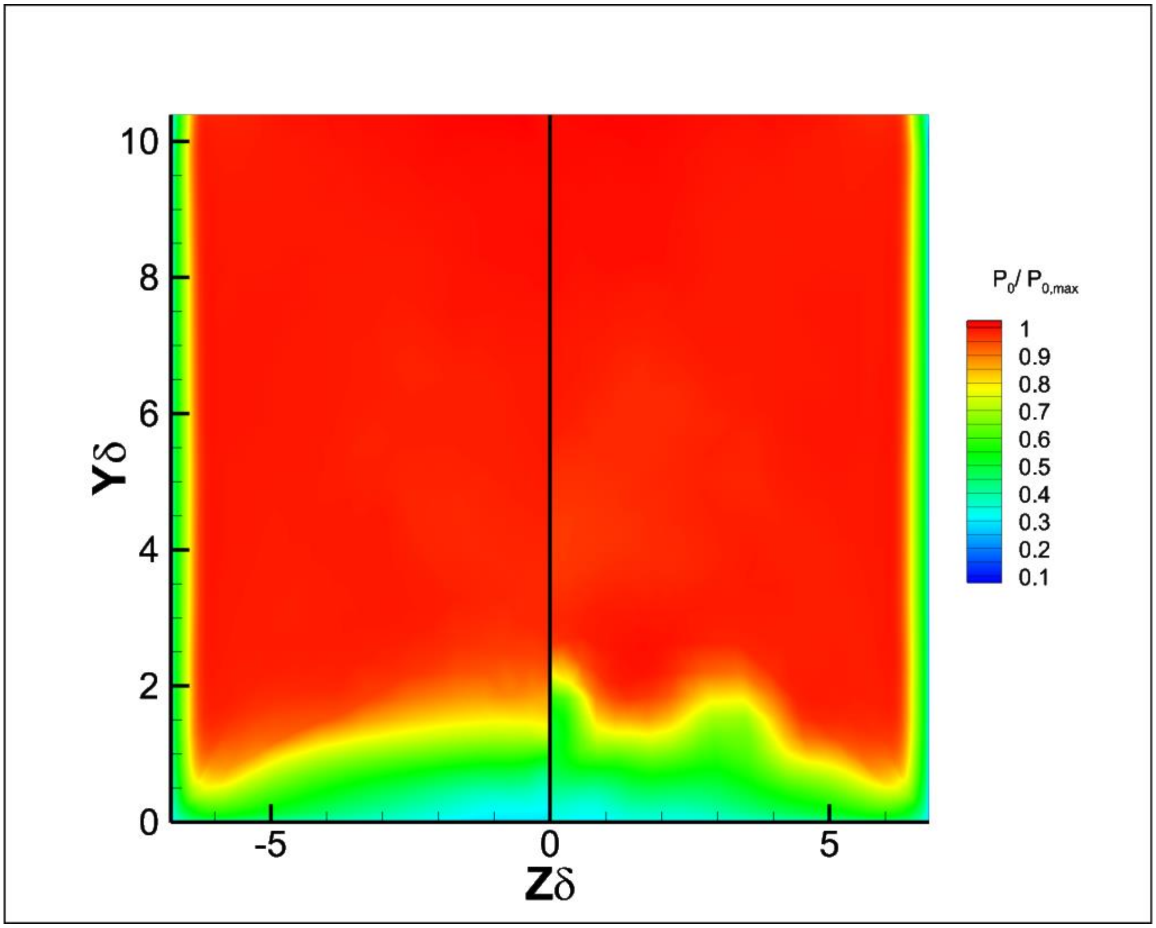

Figure 4.33 Outlet stagnation pressures without VGs (left) and with VGs (right).

CHAPTER FIVE

CONCLUSIONS

A numerical study was conducted to study the impact of Reynolds number, stagnation temperature, and gas and wall thermal models on the bulk flow distortion at M = 4.961. The main parameters observed were distortion area, distortion width, and a distortion coefficient. These variables were defined as an easily comparable metric that is representative of the distortion at the outlet.

Reynolds number appeared to have an inverse linear relationship with distortion. For each case in the test matrix, as Reynolds number was increased, distortion decreased. Another noticeable trend was that increasing stagnation temperature also decreased distortion.

Observing wall thermal models with a freestream stagnation temperature of 427K showed only slight differences between adiabatic walls and an isothermal wall with a set wall temperature of 298K at a constant Reynolds number. When the freestream stagnation temperature was set to 1280K, however, there were significant differences between an adiabatic wall and an isothermal wall with a wall temperature of 298K. The isothermal wall temperatures were colder than the freestream stagnation temperature for all cases, and each had lower distortion than their comparing adiabatic wall cases. This is consistent with previous literature findings that found that a lower wall temperature to recovery temperature ratio resulted in a smaller interaction and a thinner boundary layer.

Since the results suggested temperature was related to distortion, the relationship between static temperatures in the boundary layer and distortion was observed. All of the data for each freestream stagnation temperature collapsed into a common trend when distortion was plotted against the static temperature extracted within the co-rotating vortices that are characteristic of this interaction. Interestingly, the hottest boundary layer temperature upstream of the interaction had the coldest temperatures at this extraction location which was after the interaction. Wall cooling has been considered as a potential flow control method, and these results do agree with this method, however there is a potential for wall heating in this location to be used as a flow control method. Future work would be needed to confirm this.

Counterintuitively, the cases with the lowest distortion had the highest momentum losses between the inlet and outlet. As distortion has been noted as a cause of unstart, a compromise between ensuring safe distortion levels without overly detracting from inlet efficiency must be made. This work will contribute characterizing distortion levels at different conditions.

A calorically imperfect gas model was also utilized for the highest temperature case examined. For this case, with a freestream unit Reynolds number of 60.0×10^{6} m^{-1} and a stagnation temperature of 1280K, the temperature was not hot enough for significant amounts of calorically imperfect gas effects to take place. Although the calorically imperfect gas case did have slightly lower distortion than the comparing perfect gas case, the difference was negligible, and running the more computationally expensive calorically imperfect gas model is not recommended for distortion studies at these temperatures.

A slightly colder isothermal wall case was also studied. Since a secondary objective of the current work was to determine any uncertainties associated with ground-to-flight extrapolation, a case with a wall temperature of 273K was compared to a wall temperature of 298K for the $Re = 36.5 \times 10^{6}$ m^{-1} and $T_0 = 427K$ case. This was studied as wind tunnel facilities may experience different thermal conditions since they are thermally massive structures that may be exposed to uncontrolled climates. The results showed that for distortion studies, these small temperature changes are negligible. Future studies should explore larger wall temperature differences to draw more complete conclusions on this factor.

Another objective of this campaign was to study the effect of vortex generators in delaying separation for this interaction. A dual experimental/computational campaign was performed at M=2.01, in which the mean features observed using the two methodologies were in excellent agreement. Experimental oil flow and numerical surface streamlines were nearly identical. Both campaigns demonstrated that the use of vortex generators delayed separation, however, placing the vortex generators too close to the interaction was seen to have detrimental effects. Although separation was delayed, stagnation pressure losses were increased by the additional blockage to the flowfield. The use of these devices may assist in the prevention of unstart in a hypersonic inlet, however VGs may reduce the overall efficiency.

It is intended that this work will assist ongoing and future work in understanding distortion generated by high-speed inlets. It may also assist in determining the uncertainty associated with distortion by defining distortion's sensitivities to wall thermal models, Reynolds number, and stagnation temperature. VGs were also shown to be an effective way to delay separation in crossing-shock interactions; however, it was shown that they are detrimental to the inlet efficiency.

LIST OF REFERENCES

[1] Schmisseur, J. D., “Hypersonics into the 21st century: A perspective on AFOSR-sponsored research in aerothermodynamics,” *Progress in Aerospace Sciences*, vol. 72, 2015, pp. 3–16.

[2] Kim, H.-D., Matsuo, K., and Setoguchi, T., “Investigation on onset of shock-induced separation,” *Shock Waves*, vol. 6, Nov. 1996, pp. 275–286.

[3] Babinsky, H., Li, Y., and Pitt Ford, C. W., “Microramp Control of Supersonic Oblique Shock-Wave/Boundary-Layer Interactions,” *AIAA Journal*, vol. 47, 2009, pp. 668–675.

[4] Titchener, N., and Babinsky, H., “Shock Wave/Boundary-Layer Interaction Control Using a Combination of Vortex Generators and Bleed,” *AIAA Journal*, vol. 51, 2013, pp. 1221–1233.

[5] Hank, J. M., Murphy, J. S., and Mutzman, R. C., “The X-51A Scramjet Engine Flight Demonstration Program,” 2008, pp. 1–13.

[6] Holden, H. A., and Babinsky, H., “Effect of Microvortex Generators On Seperated Normal Shock/ Boundary Layer Interactions,” *Journal of Aircraft*, vol. 44, 2007, pp. 170–174.

[7] Dolling, D. S., “Fifty years of shock-wave/boundary-layer interaction research - What next?,” *AIAA Journal*, vol. 39, 2001, pp. 1517–1531.

[8] Volpiani, P. S., Bernardini, M., and Larsson, J., “Effects of a nonadiabatic wall on supersonic shock/boundary-layer interactions,” *Physical Review Fluids*, vol. 083401, 2018, pp. 1–21.

[9] Bernardini, M., Asproulias, I., Larsson, J., Pirozzoli, S., and Grasso, F., “Heat transfer and wall temperature effects in shock wave turbulent boundary layer interactions,” *Phys. Rev. Fluids*, vol. 1, Dec. 2016, p. 84403.

[10] Riley, L. P., Hagenmaier, M. A., Donbar, J. M., and Gaitonde, D. V., “A Computational Investigation of Unstart in a Dual-Mode Scramjet,” *54th AIAA Aerospace Sciences Meeting*, 2016, pp. 1–17.

[11] Tam, C.-J., Hsu, K.-Y., Hagenmaier, M., and Raffoul, C., “Studies of Inlet Distortion in a Direct-Connect Axisymmetric Scramjet Isolator,” *Journal of Propulsion and Power*, vol. 29, 2013, pp. 1382–1390.

[12] Nguyen, T., Vukovic, M., Behr, M., and Reinartz, B., “Numerical Simulations of Successive Distortions in Supersonic Turbulent Flow,” *AIAA Journal*, vol. 50, 2012, pp. 2365–2375.

[13] Riley, L. P., Gaitonde, D. V., Hagenmaier, M. A., and Donbar, J. M., “Isolator Dynamics During Unstart of a Dual-Mode Scramjet,” *Journal of Propulsion and Power*, 2018, pp. 1–19.

[14] Gaitonde, D. V, “Progress in Shock Wave/Boundary Layer Interactions,” *43rd Fluid Dynamics Conference*, American Institute of Aeronautics and Astronautics, 2013.

[15] Schmisseur, J. D., and Gaitonde, D. V, “Numerical Investigation of Strong Crossing Shock-Wave / Turbulent Boundary-Layer Interactions Introduction,” vol. 39, 2001.

[16] Alvi, F. S., and Settles, G. S., “Physical model of the swept shock

wave/boundary-layer interaction flowfield," *AIAA Journal*, vol. 30, 1992, pp. 2252–2258.

[17] Settles, G. S., Perkins, J. J., and Bogdonoff, S. M., "Investigation of Three-Dimensional Shock/Boundary-Layer Interactions at Swept Compression Corners," *AIAA Journal*, vol. 18, 1980, pp. 779–785.

[18] Panaras, A. G., "Review of the Physics of Swept-Shock / Boundary Layer Interactions," *Progress in Aerospace Sciences*, vol. 32, 1996, pp. 173–244.

[19] Fré, dé, Thivet, ric, Knight, D. D., Zheltovodov, A. A., and Maksimov, A. I., "Insights in Turbulence Modeling for Crossing-Shock-Wave/Boundary-Layer Interactions," *AIAA Journal*, vol. 39, 2001, pp. 985–995.

[20] Garrison, T. J., Settles, G. S., Narayanswami, N., and Knight, D., "Structure of crossing-shock-wave/turbulent-boundary-layer interactions," *AIAA Journal*, vol. 31, Dec. 1993, pp. 2204–2211.

[21] Knight, D., Yan, H., Panaras, A. G., and Zheltovodov, A., "Advances in CFD prediction of shock wave turbulent boundary layer interactions," vol. 39, 2003, pp. 121–184.

[22] GARRISON, T., SETTLES, G., NARAYANSWAMI, N., and KNIGHT, D., "Structure of crossing-shock wave/turbulent boundary-layer interactions," *28th Joint Propulsion Conference and Exhibit*, American Institute of Aeronautics and Astronautics, 1992.

[23] GARRISON, T., and SETTLES, G., "Interaction strength and model geometry effects on the structure of crossing-shock wave/turbulent boundary-layer interactions," *31st Aerospace Sciences Meeting*, American Institute of Aeronautics and Astronautics, 1993.

[24] Gaitonde, D. V., Shang, J. S., Garrison, T. J., Zheltovodov, A. A., and Maksimov, A. I., "Three-Dimensional Turbulent Interactions Caused by Asymmetric Crossing-Shock Configurations," *AIAA Journal*, vol. 37, 1999, pp. 1602–1608.

[25] DUNN, S., "Ground testing techniques in support of flight test," *Orbital Debris Conference: Technical Issues andFuture Directions*, American Institute of Aeronautics and Astronautics, 1990.

[26] Lee, K., Lee, B., Kang, S., Yang, S., and Lee, D., "Inlet Distortion Test with Gas Turbine Engine in the Altitude Engine Test Facility," *27th AIAA Aerodynamic Measurement Technology and Ground Testing Conference*, American Institute of Aeronautics and Astronautics, 2010.

[27] Gruber, M., Hagenmaier, M., and Mathur, T., "Simulating Inlet Distortion Effects in a Direct-Connect Scramjet Combustor," *42nd AIAA/ASME/SAE/ASEE Joint Propulsion Conference & Exhibit*, American Institute of Aeronautics and Astronautics, 2006.

[28] Baurle, R. A., and Axdahl, E. L., "Uncertainty Quantification of CFD Data Generated for a Model Scramjet Isolator Flowfield," 2019.

[29] BACK, L. H., and CUFFEL, R. F., "Shock wave/turbulent boundary-layer interactions with and without surface cooling," *AIAA Journal*, vol. 14, Apr. 1976, pp. 526–532.

[30] Schülein, E., “Skin Friction and Heat Flux Measurements in Shock/Boundary Layer Interaction Flows,” *AIAA Journal*, vol. 44, Aug. 2006, pp. 1732–1741.
[31] SPAID, F. W., and FRISHETT, J. C., “Incipient Separation of a Supersonic, Turbulent Boundary Layer, Including Effects of Heat Transfer,” *AIAA Journal*, vol. 10, Jul. 1972, pp. 915–922.
[32] Yentsch, R. J., and Gaitonde, D. V, “Numerical Investigation of the HIFiRE-2 Scramjet Flowpath,” *51st AIAA Aerospace Sciences Meeting*, 2013, pp. 1–45.
[33] Neuenhahn, T., *Investigation of the shock wave/boundary layer interaction of scramjet intake flows*, 2010.
[34] Im, S. kyun, and Do, H., “Unstart phenomena induced by flow choking in scramjet inlet-isolators,” *Progress in Aerospace Sciences*, vol. 97, 2018, pp. 35–60.
[35] Tan, H.-J., Li, L.-G., Wen, Y.-F., and Zhang, Q.-F., “Experimental Investigation of the Unstart Process of a Generic Hypersonic Inlet,” *AIAA Journal*, vol. 49, 2011, pp. 279–288.
[36] Herrmann, D., Blem, S., and Gülhan, A., “Experimental Study of Boundary-Layer Bleed Impact on Ramjet Inlet Performance,” vol. 27, 2011.
[37] Slater, J. W., and Saunders, J. D., “Modeling of Fixed-Exit Porous Bleed Systems for Supersonic Inlets,” *Journal of Propulsion and Power*, vol. 26, 2010, pp. 193–202.
[38] Mccormick, D. C., “Shock/Boundary-Layer Interaction Control with Vortex Generators and Passive Cavity,” vol. 31, 1993.
[39] Verma, S. B., and Manisankar, C., “Control of Incident Shock-Induced Separation Using Vane-Type Vortex-Generating Devices,” *AIAA Journal*, vol. 56, 2018, pp. 1600–1615.
[40] MCCORMICK, D. C., “Shock/boundary-layer interaction control with vortex generators and passive cavity,” *AIAA Journal*, vol. 31, 1993, pp. 91–96.
[41] Anderson, B. H., and Gibbt, J., “Study on Vortex Generator Flow Control for the Management of Inlet Distortion,” vol. 9, 1993.
[42] Lee, S., and Loth, E., “Supersonic Boundary Layer Interactions with Various Micro - Vortex Generator Geometries,” *AIAA Paper 2009 - 3712*, 2009.
[43] Cohen, G. S., and Motallebi, F., “Influence of the height of the vortex generators in the control of shock-induced separation of the boundary layers,” *Aeronautical Journal*, vol. 112, 2008, pp. 415–420.
[44] Xie, W., Wu, Z., Yu, A.-Y., and Guo, S., “Control of Severe Shock-Wave/Boundary-Layer Interactions in Hypersonic Inlets,” *Journal of Propulsion and Power*, vol. 34, 2018, pp. 614–623.
[45] Baydar, E., Lu, F. K., Slater, J. W., and Trefny, C., “Vortex Generators in a Streamline-Traced, External-Compression Supersonic Inlet,” *55th AIAA Aerospace Sciences Meeting*, 2017, p. 1383.
[46] Blinde, P. L., Humble, R. A., van Oudheusden, B. W., and Scarano, F.,

"Effects of micro-ramps on a shock wave/turbulent boundary layer interaction," *Shock Waves*, vol. 19, 2009, p. 507.

[47] Verma, S. B., Manisankar, C., and Raju, C., "Control of shock unsteadiness in shock boundary-layer interaction on a compression corner using mechanical vortex generators," *Shock Waves*, vol. 22, 2012, pp. 327–339.

[48] Interaction, B., and Lee, S., "Impact of Ramped Vanes on Normal Shock," vol. 50, 2012.

[49] Anderson, B., Tinapple, J., and Surber, L., "Optimal control of shock wave turbulent boundary layer interactions using micro-array actuation," *3rd AIAA Flow Control Conference*, 2006, p. 3197.

[50] Deceased, H. S., *Boundary- Layer Theory*.

[51] Godunov, S. K., "A difference method for numerical calculation of discontinuous solutions of the equations of hydrodynamics," *Matematicheskii Sbornik*, vol. 89, 1959, pp. 271–306.

[52] Tomaro, R., Strang, W., Sankar, L., Tomaro, R., Strang, W., and Sankar, L., "An implicit algorithm for solving time dependent flows on unstructured grids," *35th Aerospace Sciences Meeting and Exhibit*, 1997, p. 333.

[53] Spalart, P., and Allmaras, S., "A one-equation turbulence model for aerodynamic flows," *30th aerospace sciences meeting and exhibit*, 1992, p. 439.

[54] Mani, M., Babcock, D., Winkler, C., and Spalart, P., "Predictions of a Supersonic Turbulent Flow in a Square Duct," *51st AIAA Aerospace Sciences Meeting including the New Horizons Forum and Aerospace Exposition*, 2013, pp. 1–19.

[55] Nichols, R. H., "A Summary of the Turbulence Models in the CREATE-AV Kestrel Flow Solvers," *AIAA Scitech 2019 Forum*, American Institute of Aeronautics and Astronautics, 2019.

[56] Rumsey, C., "3DSSD: 3D Supersonic Square Duct Validation Case," *NASA Turbulence Modeling Resource* Available: https://turbmodels.larc.nasa.gov/3dsqduct_val.html.

[57] DAVIS, D. O., and GESSNER, F. B., "Further experiments on supersonic turbulent flow development in a square duct," *AIAA Journal*, vol. 27, Aug. 1989, pp. 1023–1030.

[58] Lindorfer, S. A., "A Numerical Study of the Limiting Cases of Cylinder-Induced Shock Wave / Boundary Layer Interactions," 2017.

[59] Schmisseur, J. D., and Gaitonde, D. V, "Numerical Investigation of Strong Crossing Shock-Wave/Turbulent Boundary-Layer Interactions," *AIAA Journal*, vol. 39, Sep. 2001, pp. 1742–1749.

[60] Zheltovodov, A. A., and Maksimov, A. I., *Hypersonic Crossing Shock-Waves/Turbulent Boundary Layer Interaction*, RUSSIAN ACADEMY OF SCIENCES NOVOSIBIRSK INST OF THEORETICAL AND APPLIED …, 1999.

[61] Combs, C. S., Lash, E. L., and Schmisseur, J. D., "Investigation of a

Cylinder-Induced Transitional Shock Wave-Boundary Layer Interaction using Laser Diagnostics," *32nd AIAA Aerodynamic Measurement Technology and Ground Testing Conference*, American Institute of Aeronautics and Astronautics, 2016.

[62] Kocher, B. D., Combs, C. S., Kreth, P. A., and Schmisseur, J. D., "Investigation of the Effects of Ablation-Induced Roughness on Supersonic Flows," *47th AIAA Fluid Dynamics Conference*, American Institute of Aeronautics and Astronautics, 2017.

[63] Lash, E. L., Combs, C. S., Kreth, P. A., and Schmisseur, J. D., "Experimental Investigation of a Cylinder-Induced Transitional Shock Wave-Boundary Layer Interaction," *55th AIAA Aerospace Sciences Meeting*, 2017, pp. 1–22.

[64] Settles, G., and Dolling, D., "Swept shock/boundary-layer interactions - Tutorial and update," *28th Aerospace Sciences Meeting*, American Institute of Aeronautics and Astronautics, 1990.

[65] Lee, S., and Loth, E., "On ramped vanes to control normal shock boundary layer interactions," *The Aeronautical Journal*, vol. 122, 2018, pp. 1568–1585.

[66] Kimmel, R. L., and Adamczak, D., "HIFiRE-5 Flight Vehicle Design," 2019, pp. 1–17.

[67] Holden, M. S., Maclean, M., Wadhams, T. P., and Dufrene, A., "Measurements of Real Gas Effects on Regions of Laminar Shock Wave / Boundary Layer Interaction in Hypervelocity Flows for " Blind ' Code Validation Studies Introduction and Review of Earlier Studies Laminar Shock Interactions in," 2013, pp. 1–14.

[68] Introduction, I., "Interpolation Methods for Inlet Distortion Determination," 2016, pp. 1–13.

[69] Field, M., "Investigation of a hypersonic crossing shock wave/turbulent boundary layer interaction," vol. 2, 1993, pp. 35–48.

[70] Bernardini, M., Asproulias, I., Larsson, J., Pirozzoli, S., and Grasso, F., "Heat transfer and wall temperature effects in shock wave turbulent boundary layer interactions," *Physical Review Fluids*, vol. 1, 2016, pp. 1–18.

[71] Ghosh, S., Choi, J.-I., and Edwards, J. R., "Numerical Simulations of Effects of Micro Vortex Generators Using Immersed-Boundary Methods," *AIAA Journal*, vol. 48, 2010, pp. 92–103.

VITA

Matthew Schwartz was born and raised in Nashville, TN to Richard and Catherine Schwartz. Matthew received a Bachelor of Science in Aerospace Engineering at the University of Tennessee, Knoxville in May of 2017. Matthew continued his Aerospace education at the University of Tennessee Space Institute in Tullahoma for his Master of Science degree.